Frontiers in Bioscience Landmark

Front. Biosci. (Landmark Ed) **2026**; 31(11): 56745
https://doi.org/10.31083/FBL56745

Original Research

TIMP1 Expression and NK Cell-Related Immune Heterogeneity in Colorectal Cancer

Ziqing Zhang[1,2,†], Zhangqi Cao[1,†], Haoyan Li[3], Mingjiang Mo[3], Yang Gao[4], Hanqing Chen[5], Bei Zhang[1,*], Mengping Li[1,*]

[1]TCM&VIP Department, Guangdong Provincial Clinical Research Center for Cancer, State Key Laboratory of Oncology in South China, Sun Yat-sen UniversityCancer Center, 510060 Guangzhou, Guangdong, China
[2]Department of Oncology, Guangdong Provincial Hospital of Chinese Medicine; The Second Affiliated Hospital of Guangzhou University of Chinese Medicine; Guangdong Provincial Academy of Chinese Medical Sciences, 510120 Guangzhou, Guangdong, China
[3]School of Clinical Integrative Chinese and Western Medicine, The Affiliated Traditional Chinese Medicine Hospital of Guangzhou Medical University, Guangzhou Medical University, 510130 Guangzhou, Guangdong, China
[4]Guangzhou Medical University-Guangzhou Institute of Biomedicine and Health, Chinese Academy of Sciences, School of Life Sciences, Guangzhou Medical University, 511436 Guangzhou, Guangdong, China
[5]Beijing Key Laboratory of Environment and Aging, Department of Nutrition and Food Hygiene, School of Public Health, Capital Medical University, 100069 Beijing, China
*Correspondence: zhangbei@sysucc.org.cn (Bei Zhang); limp@sysucc.org.cn (Mengping Li)
[†]These authors contributed equally.
Academic Editor: Sukmook Lee
Submitted: 5 August 2026 Revised: 9 October 2026 Accepted: 13 October 2026 Published: 12 November 2026

Abstract

Background: Microsatellite instability (MSI) captures only part of the immune heterogeneity in colorectal cancer (CRC). We investigated natural killer (NK) cell-related expression patterns and their relationship with tissue inhibitor of metalloproteinases 1 (TIMP1). **Methods:** We analyzed TCGA-COAD expression and clinical data and assessed TIMP1 expression in two independent cohorts, HTAN-MSK and GSE14333. Single-cell data from GSE178318 were used to map TIMP1 expression across cell populations. Quantitative real-time PCR (qRT-PCR) and western blotting were used to compare TIMP1 mRNA and protein levels, respectively, in NCM460 and HCT116 cells. Virtual knockout, splicing analysis, and compound screening provided exploratory predictions. **Results:** An 11-gene expression signature stratified patients according to survival and immune-stromal features. Independent cohorts showed higher TIMP1 expression in primary and metastatic CRC than in matched normal tissues and an association with shorter disease-free survival. HCT116 cells exhibited higher TIMP1 mRNA and protein levels than NCM460 cells. Single-cell analysis detected TIMP1 expression across NK, myeloid, endothelial, epithelial, and other immune cell populations. Three splicing events differed according to MSI status, and virtual knockout analysis predicted immune-related expression changes. Compound screening identified BRD-A98990573 as a candidate for experimental testing. **Conclusions:** TIMP1 expression is associated with adverse prognosis and multicellular immune-stromal features in CRC. Findings from independent cohorts and cellular expression analyses support further investigation of TIMP1.

Keywords: colorectal neoplasms; tissue inhibitor of metalloproteinase-1; killer cells, natural; tumor microenvironment; microsatellite instability; single-cell gene expression analysis

1. Introduction

Colorectal cancer (CRC) remains a leading cause of cancer death worldwide [1]. Its clinical behavior and treatment response vary with molecular subtype and immune composition [2,3,4]. Deficient mismatch repair (dMMR) or high microsatellite instability (MSI-H) is commonly accompanied by increased mutational burden, neoantigen formation, and immune infiltration [3,5,6]. These features help explain greater sensitivity to immune checkpoint blockade (ICB) than in most mismatch repair-proficient (pMMR) or microsatellite-stable (MSS) tumors [4,6,7,8,9]. MSI status nevertheless captures only part of the variation in tumor immunity. Additional biological features could help characterize this heterogeneity and refine patient stratification.

CRC immunotherapy is usually interpreted through T-cell activation and exhaustion because current checkpoint treatments target PD-1 and CTLA-4 [10,11,12]. Natural killer (NK) cells provide complementary tumor recognition by responding to cellular stress and altered major histocompatibility complex class I expression without antigen-specific priming [13,14,15]. Single-cell studies have identified diverse NK-cell and innate lymphoid states in CRC [16,17,18]. These findings motivated an NK cell-related starting point for our analysis of immune heterogeneity. This analytical focus does not assume that TIMP1 acts selectively on NK cells or that other immune populations are less important.

Alternative splicing (AS) adds information about transcript processing beyond measurements of total gene ex-

Copyright: © 2026 The Author(s). Published by IMR Press.
This is an open access article under the CC BY 4.0 license.

Publisher's Note: IMR Press stays neutral with regard to jurisdictional claims in published maps and institutional affiliations.

pression. It can influence antigen presentation, immune recognition, and treatment response [19,20,21], and CRC splicing patterns have been associated with immune infiltration [22]. We examined TIMP1 splice events alongside MSI status and total expression as a secondary analysis. This approach describes transcript variation without presupposing a splice-dependent mechanism of NK-cell regulation.

Tissue inhibitor of metalloproteinases 1 (TIMP1) is a secreted protein with metalloproteinase-inhibitory and signaling functions [23,24]. Circulating and tissue TIMP1 levels have been associated with CRC detection and patient outcomes [25,26,27]. Experimental studies have implicated TIMP1 in fibroblast accumulation and colon cancer proliferation and invasion [23,24]. Its clinical relevance has also been reported in colorectal liver metastasis [28]. These observations place TIMP1 within tumor-stromal biology, but its relationship with NK cell-associated features in CRC remains less clear.

We examined NK cell-related expression patterns in TCGA-COAD and evaluated TIMP1 across independent cohorts, single-cell data, and cultured cells (Fig. 1). The 11-gene signature was based on gene expression, not splice-event measurements. External cohorts assessed TIMP1 expression and prognosis; RT-qPCR and western blotting measured total TIMP1 in NCM460 and HCT116 cells. Single-cell analyses described its cellular distribution and associations with NK-cell transcriptional states. Splicing and compound analyses were retained as exploratory components rather than tests of a regulatory mechanism.

2. Materials and Methods

2.1 Data Acquisition and Preprocessing

FPKM-normalized RNA-expression matrices and clinicopathological records were downloaded from The Cancer Genome Atlas (TCGA; https://portal.gdc.cancer.gov). Ensembl supplied the human gene annotations. Percent spliced-in (PSI) measurements and AS-event records were retrieved from TCGASpliceSeq (https://bioinformatics.mdanderson.org/TCGASpliceSeq/PSIdownload.jsp) [29]. Matching the expression, splicing, survival, and clinical files yielded 434 patients for the principal prognostic analyses.

2.2 Identification of NK Cell-Associated Genes and AS Features

Co-expression modules related to CRC and immune traits were derived with weighted gene co-expression network analysis (WGCNA) [30]. We intersected differentially expressed genes, overall-survival (OS)-associated genes, and genes related to NK-cell traits, which produced 58 candidates. AS records were linked to their host genes for gene-level interpretation. Univariate Cox models provided prognostic screening, and Spearman coefficients quantified NK-cell associations. Analyses and graphics used DESeq2, WGCNA, clusterProfiler, org.Hs.eg.db, tidygraph, ggraph, ggplot2, and forestplot as appropriate.

2.3 Construction and Internal Evaluation of an 11-Gene Prognostic Expression Signature

Within the training data, each of the 58 candidates was first examined by univariate Cox regression. Variable reduction used a least absolute shrinkage and selection operator (LASSO) Cox model with 10-fold cross-validation [31,32], after which a multivariable Cox model was fitted. Eleven genes remained: *S1PR5*, *TIMD4*, *XCL1*, *HSF4*, *ERFE*, *NKX6-3*, *TIMP1*, *CXXC5*, *SALL1*, *CPT2*, and *CD1A*. For every patient, normalized expression of each gene was multiplied by its Cox coefficient and the products were summed to obtain the risk score. The median defined the two risk groups. A random 60:40 split generated Train and Test subsets; because both originated from TCGA-COAD, the Test subset represented internal rather than external validation. Kaplan-Meier curves, ordered risk plots, expression heatmaps, and receiver operating characteristic analyses were used for internal assessment.

2.4 Nomogram Construction

Age, tumor stage, and the expression-derived risk score were entered into a prognostic nomogram. Harrell's concordance index measured discrimination. Agreement and potential clinical utility were examined with calibration plots, decision-curve analysis, and clinical-impact curves across relevant threshold probabilities.

2.5 Tumor Microenvironment Analysis

Cell-type identification by estimating relative subsets of RNA transcripts (CIBERSORT) and single-sample gene set enrichment analysis (ssGSEA) provided complementary estimates of immune-cell composition [33,34]. Spearman coefficients related the risk score to immune measurements. Pathway activity, checkpoint-gene expression, and cancer-immunity-cycle scores were then contrasted between risk groups.

2.6 Computational Indicators Relevant to Immune Checkpoint Blockade

Somatic variants were summarized with maftools [35], and tumor mutational burden (TMB) was evaluated by risk group. Scores for Tumor Immune Dysfunction and Exclusion (TIDE), MSI, T-cell dysfunction, and T-cell exclusion came from the TIDE platform [36]. They were treated as computational descriptors of immune context, not as measured responses to checkpoint therapy.

2.7 TIMP1 Prioritization and Bulk Immune Association Analysis

Candidate prioritization considered four elements: tumor-normal differential expression, association with OS, agreement with the direction of the expression model, and

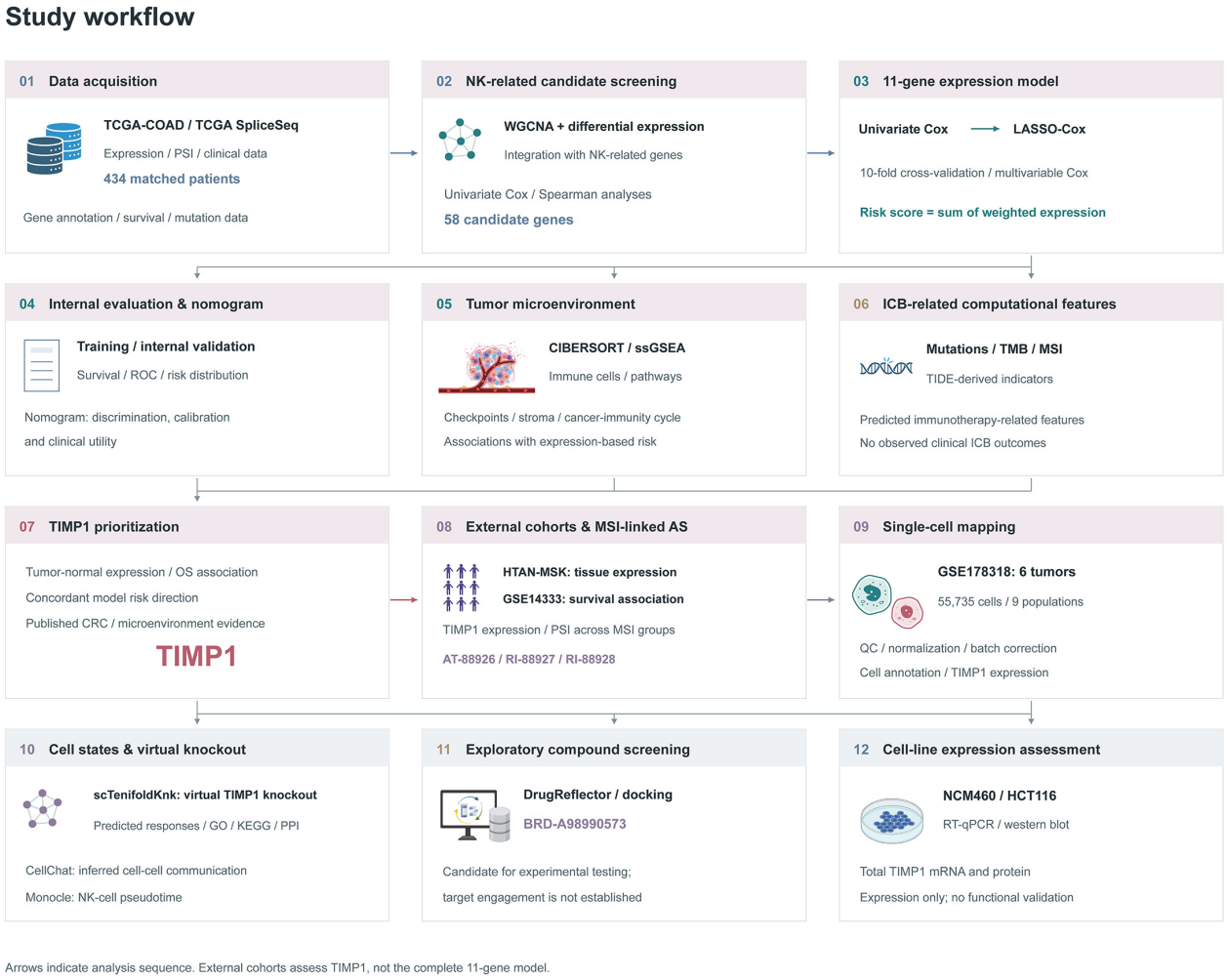


Fig. 1. Study design. TCGA-COAD expression, splicing, clinical, mutation, immune, and drug-sensitivity data were combined with external cohorts and single-cell datasets. The workflow evaluated an NK cell-related expression signature and then examined TIMP1 across MSI, prognostic, cellular, and *in silico* therapeutic contexts. TCGA-COAD, The Cancer Genome Atlas Colon Adenocarcinoma; NK, natural killer; TIMP1, tissue inhibitor of metalloproteinases 1; MSI, microsatellite instability. Created in BioRender. Zhang, Z. (2026) https://BioRender.com/xazc66m.

prior evidence in CRC or the tumor microenvironment. TCGA-COAD tumor and normal samples were used for the TIMP1 expression comparison. Spearman analyses related TIMP1 to stromal/CAF, endothelial, macrophage, NK-cytotoxicity, immune-checkpoint, regulatory-T-cell, and interferon-gamma chemokine scores.

2.8 External Validation and MSI-Associated TIMP1 Expression

External expression analysis used the HTAN-MSK CRC study (crc_hta8_htan_2024), which contains linked normal-colon, primary-tumor, and metastatic specimens. Pseudobulk mRNA values were aggregated by patient and sample class. Paired Wilcoxon signed-rank tests were followed by Benjamini-Hochberg adjustment. Prognostic assessment used GSE14333, generated on the Affymetrix Human Genome U133 Plus 2.0 Array. TIMP1 was represented by probe 201666_at; disease-free survival (DFS) was modeled with standardized continuous expression and with a median-defined grouping using Cox and log-rank analyses.

TCGA clinical annotations defined three microsatellite categories: MSS, microsatellite instability-low (MSI-L), and MSI-H. A Kruskal-Wallis test assessed overall differences in TIMP1 expression, followed by Benjamini-Hochberg-adjusted pairwise Wilcoxon comparisons.

2.9 TIMP1-Specific AS Analysis

TCGA SpliceSeq contained four *TIMP1* events: alternate terminator AT-88926, exon-skipping ES-88929, and the retained-intron events RI-88927 and RI-88928. Their PSI measurements were aligned with MSI status and total TIMP1 expression in TCGA-COAD. Kruskal-Wallis tests compared PSI across MSI categories, and Spearman analysis related event-level PSI to gene expression. Benjamini-

Hochberg correction was applied across the four events; focused plots were restricted to events retaining an MSI association after adjustment.

2.10 Single-Cell RNA-seq Preprocessing and Annotation

Six primary CRC specimens from GSE178318 were processed in Seurat [37,38]. Following cell filtering and normalization, 2000 variable genes were selected for principal-component analysis, and Harmony corrected batch effects [39]. Clusters were displayed by t-distributed stochastic neighbor embedding (t-SNE) and uniform manifold approximation and projection (UMAP). Canonical markers assigned B, endothelial, epithelial, mast, myeloid, NK, plasmacytoid dendritic, plasma, and T-cell identities.

2.11 scTenifoldKnk Virtual-Knockout Analysis

The annotated NK-cell subset was subjected to an *in silico TIMP1* knockout with scTenifoldKnk [40]. Single-cell expression profiles were used to infer gene-regulatory networks and predict TIMP1-responsive genes. Significance required $p < 0.05$ and a fold change greater than 2. Gene Ontology (GO) and Kyoto Encyclopedia of Genes and Genomes (KEGG) enrichment incorporated multiple-testing correction, and a protein-protein interaction network summarized connectivity. These outputs represent network perturbation predictions rather than observations from a physical knockout.

2.12 CellChat Analysis

CellChat inferred ligand-receptor communication among the annotated populations [41]. Global network plots summarized predicted communication strength, and bubble plots displayed selected ligand-receptor pairs. The analysis placed TIMP1-associated observations within the wider multicellular CRC environment.

2.13 Monocle Pseudotime Analysis

NK-cell state structure was reconstructed with Monocle pseudotime analysis [42,43]. Ordering genes defined the inferred trajectory, onto which TIMP1 expression was projected. The resulting ordering was interpreted as a continuum of transcriptional states and not as direct temporal or causal evidence.

2.14 Exploratory DrugReflector Screening and Molecular Docking

DrugReflector ranked compounds according to the transcriptional program associated with TIMP1 [44]. Rank, logit, and probability values were retained from its output. BRD-A98990573 was docked to TIMP1 (Protein Data Bank [PDB] ID 9SOQ) with AutoDock Vina (version 1.2.2; The Scripps Research Institute, La Jolla, CA, USA) [45]. Screening and docking were used to nominate testable candidates, not to establish binding, inhibition, or efficacy.

2.15 Cell-Based Experimental Validation of TIMP1 Expression

2.15.1 Cell Culture

NCM460 normal colonic mucosal cells (RRID: CVCL_0460) and HCT116 CRC cells (RRID: CVCL_0291) were obtained from iCell Bioscience Inc. (Shanghai, China). STR profiles matched the corresponding reference profiles, and both cultures tested negative for mycoplasma before experimentation. Cells were maintained at 37 °C and 5% CO_2 in high-glucose Dulbecco's modified Eagle's medium (DMEM; Gibco, Thermo Fisher Scientific, Cat. No. C11995500BT). The medium contained 10% fetal bovine serum (Gibco, Thermo Fisher Scientific, Cat. No. 10099141C) and 1% penicillin-streptomycin (Sigma-Aldrich, Cat. No. P4333).

2.15.2 Western Blotting

Log-phase NCM460 and HCT116 cultures were rinsed twice in ice-cold PBS (Gibco, Thermo Fisher Scientific, Cat. No. 10010023). For each 1×10^6 cells, 100–200 µL RIPA buffer (Beyotime, Cat. No. P0013B) was supplemented with 1 mM PMSF (Sigma-Aldrich, Cat. No. P7626) and 1× protease/phosphatase inhibitor cocktail (Roche, Cat. No. 04693132001). Lysis proceeded on ice for 30 min, with vortex mixing every 10 min. Lysates were centrifuged at 12,000 ×g for 15 min at 4 °C, and the resulting supernatants were retained. Protein content was measured with the Beyotime BCA kit (Cat. No. P0010). Equal protein inputs underwent 10% SDS-PAGE before wet transfer to PVDF membranes (Millipore, Cat. No. IPVH00010). RapidBlock solution (Bio-Rad, Cat. No. 12010020) was applied for 10 min. Membranes were then incubated at 4 °C overnight with anti-TIMP1 (Affinity Biosciences, Cat. No. AF5314; 1:1000) and anti-β-actin (Cell Signaling Technology, Cat. No. 4967; 1:1000). After washing, horseradish peroxidase (HRP)-conjugated secondary antibody (Abmart, Cat. No. M21002; 1:5000) was applied for 1 h at room temperature. Signals were developed with ECL substrate (Affinity Biosciences, Cat. No. KF8005), recorded on a Bio-Rad chemiluminescence system, and quantified in ImageJ (version 1.54t; National Institutes of Health, Bethesda, MD, USA).

2.15.3 Quantitative Real-Time PCR

TRIzol reagent (Thermo Fisher Scientific, Cat. No. 15596018) was used to isolate total RNA from NCM460 and HCT116 cells. Concentration and purity were measured on a NanoDrop 2000 spectrophotometer; only RNA with an A260/A280 ratio of 1.8–2.0 proceeded to reverse transcription. cDNA was prepared with the PrimeScript RT Reagent Kit (Takara Bio, Cat. No. RR037A). Reactions for quantitative real-time PCR (qRT-PCR) contained SYBR Green Master Mix (Takara Bio, Cat. No. RR420A) and were run on a QuantStudio 5 system (Thermo Fisher Scientific). *GAPDH* served as the reference transcript, and rel-

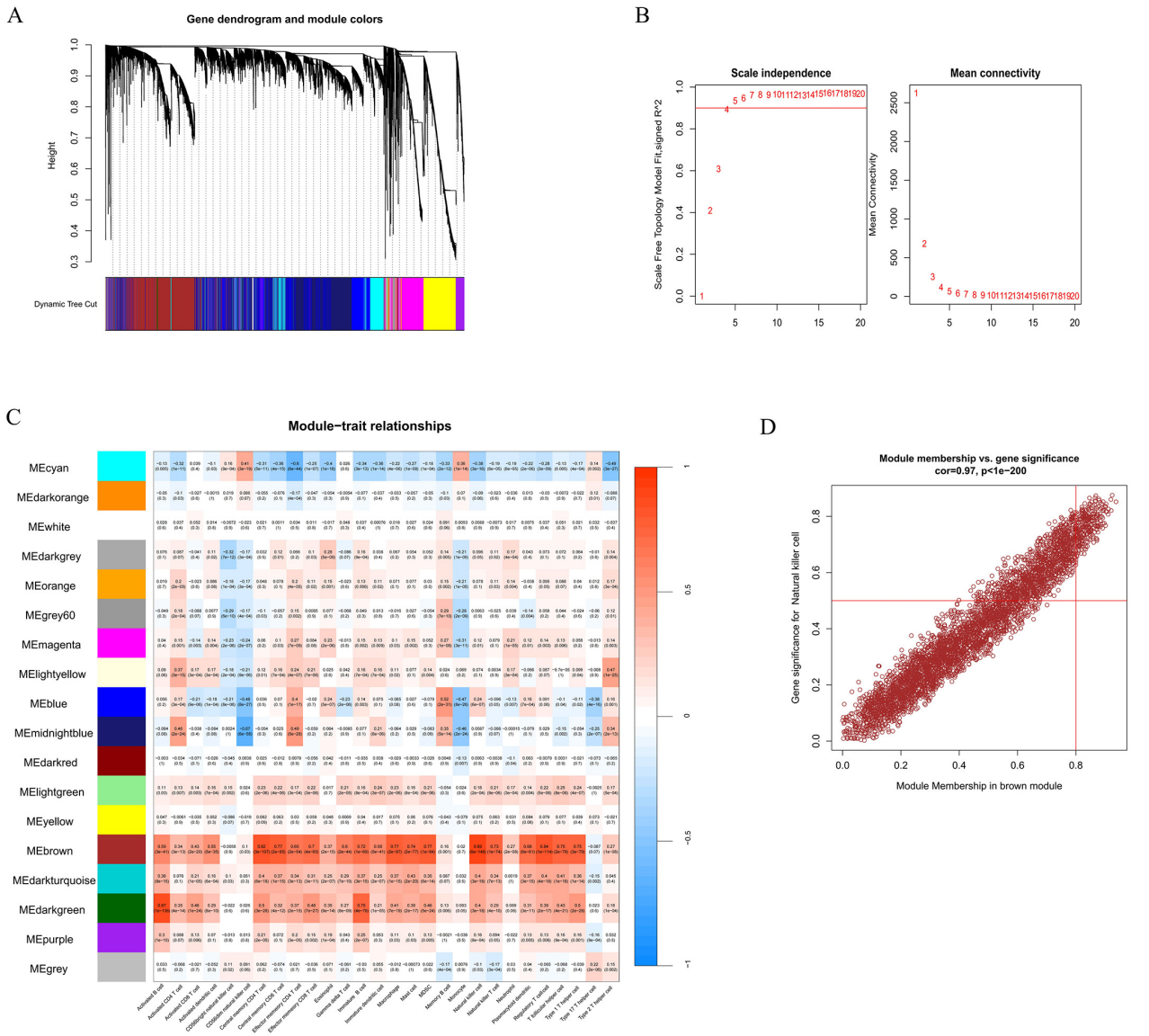


Fig. 2. CRC-associated modules identified by WGCNA. (A) Dynamic-tree-cut dendrogram with colors denoting 18 co-expression modules. (B) Scale-free topology and mean-connectivity profiles used to choose the soft threshold. (C) Correlations of modules with CRC phenotypes and immune traits; cells contain coefficients with *p*-values in parentheses, and the color scale indicates direction. (D) Relationship between module membership and NK-cell gene significance in the brown module. CRC, colorectal cancer; WGCNA, weighted gene co-expression network analysis.

ative *TIMP1* abundance was derived by the $2^{-\Delta\Delta Ct}$ method. **Supplementary Table 1** lists the primer sequences.

2.16 Statistical Analysis

Analyses were conducted in R 4.6.0 (R Foundation for Statistical Computing, Vienna, Austria) and GraphPad Prism 10.1 (GraphPad Software, Boston, MA, USA). Non-parametric group comparisons used Wilcoxon tests. Survival distributions were evaluated by Kaplan-Meier estimation and log-rank testing, while Cox models supplied hazard ratios and 95% confidence intervals. Spearman coefficients described continuous associations, and Welch's unpaired *t*-test compared the two cell lines. Related multiple tests were adjusted by the Benjamini-Hochberg procedure. Unless an adjusted criterion is stated, inference used two-sided tests with $p < 0.05$.

3. Results

3.1 CRC-Associated Co-Expression Modules

WGCNA was first applied to transcriptomes from 434 patients. Dynamic tree cutting separated 18 modules (Fig. 2A), and the selected soft threshold was compatible with scale-free topology (Fig. 2B). Of these modules, the brown

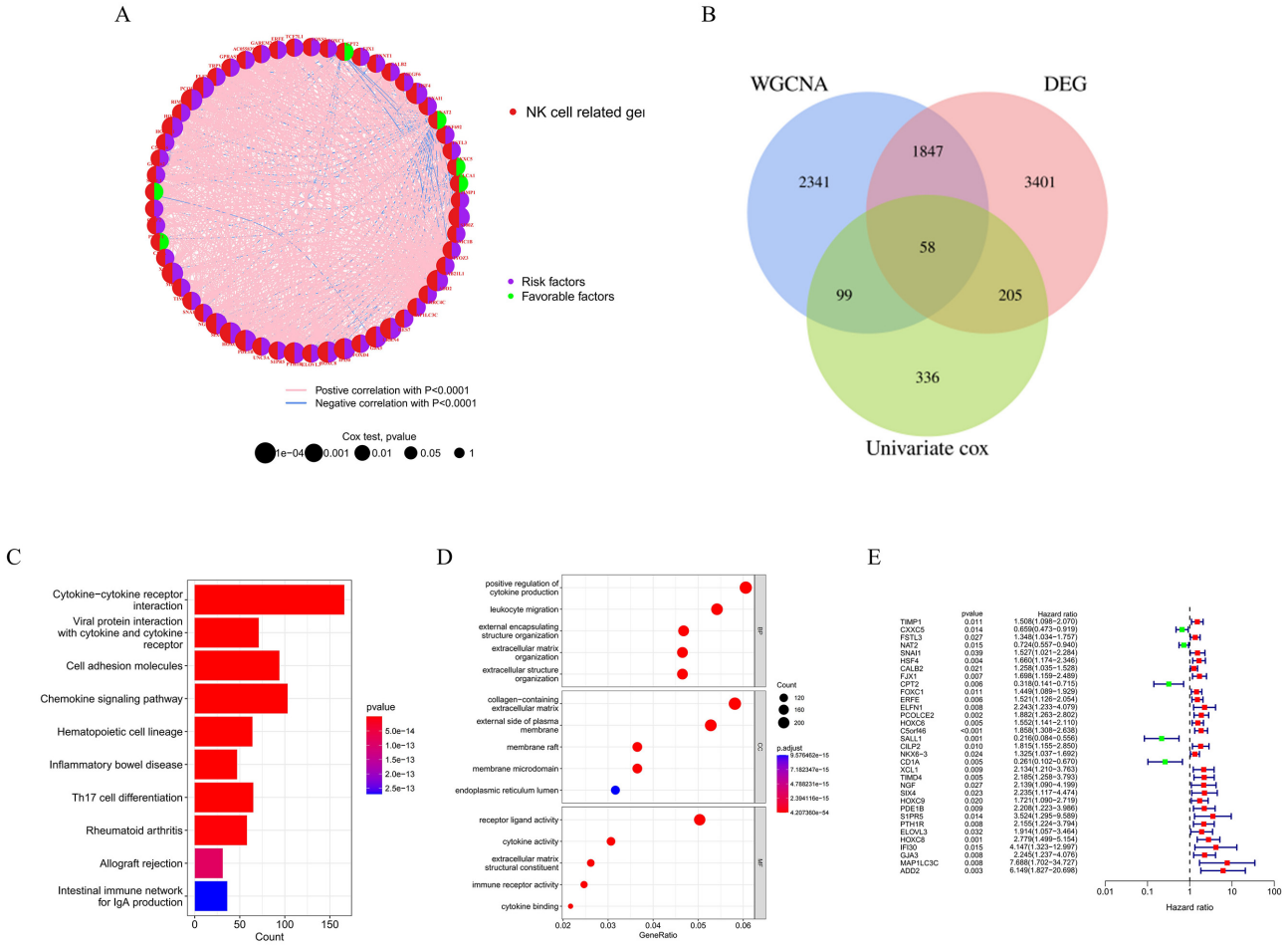


Fig. 3. Candidate-gene screening and enrichment. (A) Interaction network of NK cell-related genes. Purple and green indicate adverse and favorable survival associations, respectively, and red markers denote NK cell-related genes. Pink and blue edges represent positive and negative correlations, respectively. Node size reflects the Cox regression *p*-value. (B) Intersection of WGCNA-module, differentially expressed, and Cox-associated genes, yielding 58 candidates. (C) KEGG pathway enrichment of the candidate genes. (D) GO enrichment analysis of the candidate genes, categorized into biological process (BP), cellular component (CC), and molecular function (MF). (E) Univariate Cox estimates with HRs and 95% confidence intervals. GO, Gene Ontology; KEGG, Kyoto Encyclopedia of Genes and Genomes; HR, hazard ratio.

module showed the closest relationship with NK-cell traits (Fig. 2C). Module membership and NK-cell gene significance were strongly correlated within this module (r = 0.97, $p < 0.001$; Fig. 2D).

3.2 NK Cell-Associated Candidate Genes and Functional Programs

Intersecting WGCNA modules with differential-expression and survival screens yielded 58 NK cell-associated genes (Fig. 3A,B). KEGG analysis highlighted cytokine-receptor and chemokine pathways, cell adhesion, hematopoietic lineage, and intestinal immune processes (Fig. 3C). Their GO terms included cytokine signaling, immune regulation, and leukocyte adhesion (Fig. 3D). Cox screening produced candidates with hazard ratio (HR) values both above and below 1 (Fig. 3E).

3.3 NK Cell-Related Expression Signature and Survival

The Sankey plot related NK-associated clusters to risk classification and survival status (Fig. 4A). LASSO selection and multivariable Cox modeling retained *S1PR5*, *TIMD4*, *XCL1*, *HSF4*, *ERFE*, *NKX6-3*, *TIMP1*, *CXXC5*, *SALL1*, *CPT2*, and *CD1A* (Fig. 4B,C). Positive coefficients for S1PR5, TIMD4, XCL1, HSF4, ERFE, NKX6-3, and TIMP1 indicated greater modeled risk. *CXXC5*, *SALL1*, *CPT2*, and *CD1A* had negative coefficients.

Ordered risk and survival-status plots are presented for the Train, Test (internal-validation), and All cohorts (Fig. 4D–I), with corresponding expression heatmaps in Fig. 4J–L. OS was shorter in the high-risk group in Train (log-rank $p < 0.0001$), Test ($p = 0.002$), and All analyses ($p < 0.0001$; Fig. 4M–O). For the All cohort, time-dependent AUCs at 1, 3, and 5 years were 0.74, 0.71, and 0.68 (Fig. 4P–R). Sum-

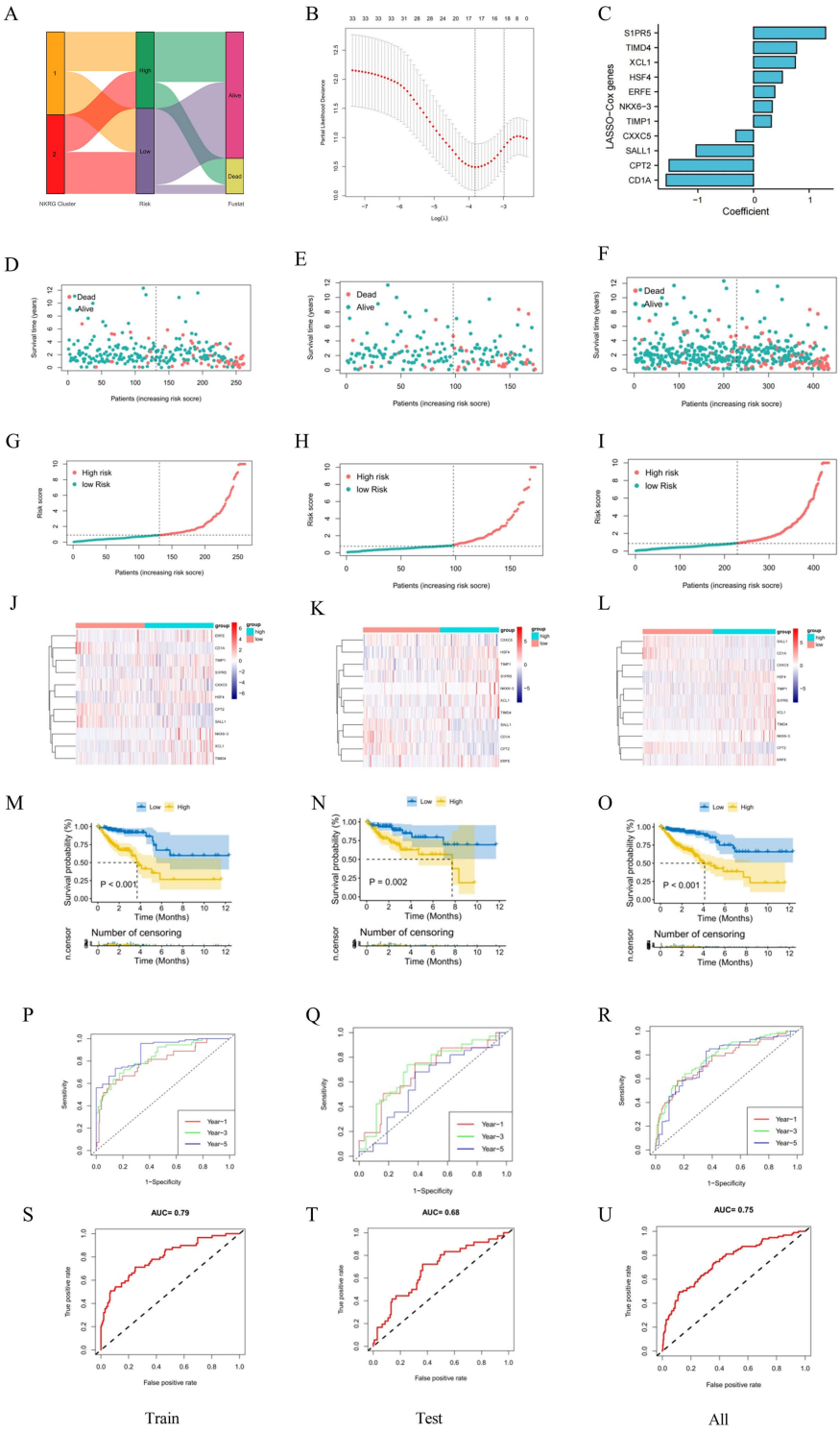


Fig. 4. Internal assessment of the 11-gene NK cell-related expression signature. (A) Links among NK-related clusters, risk groups, and survival status. (B) LASSO-Cox cross-validation and selection of lambda. (C) Coefficients of the retained genes; positive and negative values correspond to higher and lower modeled risk. (D–F) Survival status ordered by risk score in Train, Test, and All cohorts. (G–I) Risk-score distributions; dashed lines mark the median cutoff. (J–L) Expression heatmaps for the signature genes. (M–O) Kaplan-Meier OS curves. (P–R) Time-dependent ROC curves at 1, 3, and 5 years. (S–U) Summary ROC curves for Train, Test, and All. The Test cohort is an internal-validation subset of TCGA-COAD. LASSO, least absolute shrinkage and selection operator; ROC, receiver operating characteristic.

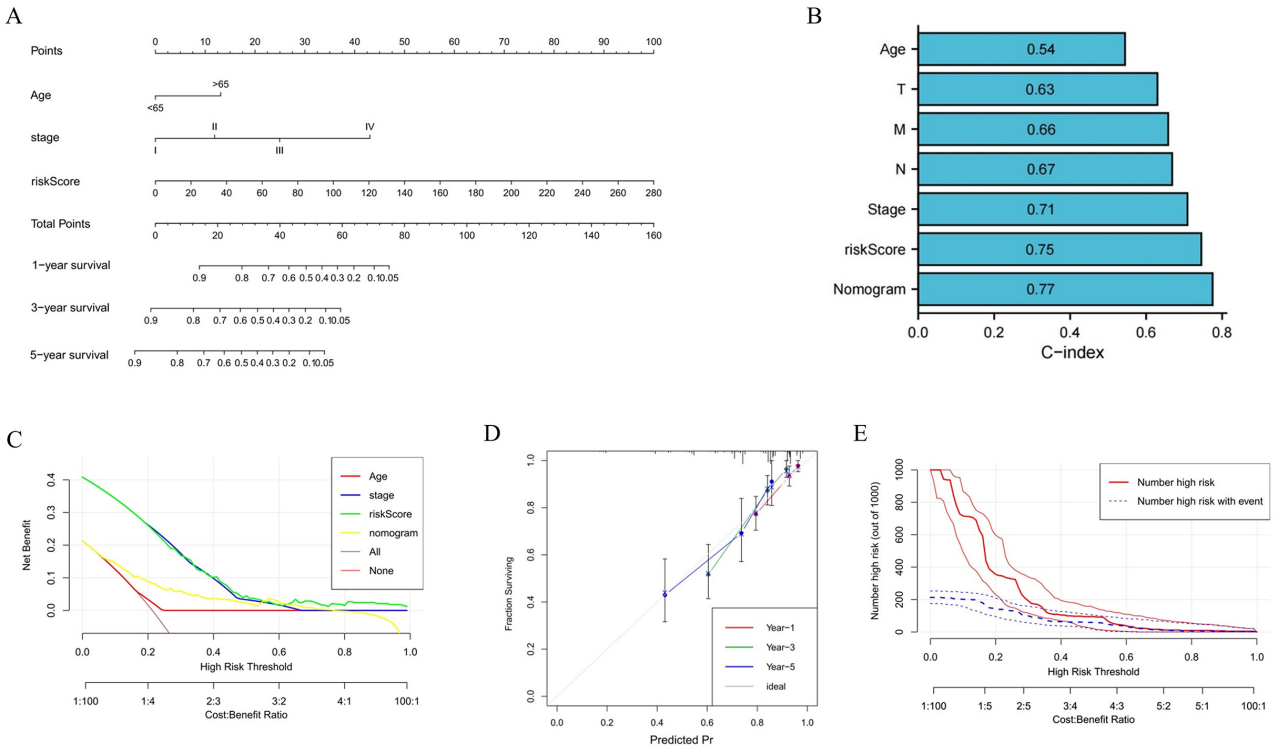


Fig. 5. Prognostic nomogram and internal evaluation. (A) Point-based estimates of 1-, 3-, and 5-year OS from age, stage, and risk score. (B) Concordance indices for the nomogram and its component predictors. (C) Decision curves at the three time points. (D) Observed versus predicted survival in calibration plots. (E) Clinical-impact analysis of the nomogram. OS, overall survival.

mary AUCs were 0.79 in Train, 0.68 in Test, and 0.75 in All (Fig. 4S–U). These results describe internal discrimination and do not constitute independent validation.

Clinicopathological heatmaps and principal component analysis further distinguished the risk groups (**Supplementary Fig. 1**). Stratified Kaplan-Meier analyses revealed similar risk directionality across several clinical subgroups (**Supplementary Fig. 2**).

3.4 Combined Clinical and Expression-Based Survival Assessment

The nomogram combined age, tumor stage, and risk score to estimate OS at 1, 3, and 5 years (Fig. 5A). Its concordance index was higher than that of any included clinical variable or the risk score alone (Fig. 5B). Calibration, decision-curve, and clinical-impact plots provided additional internal assessments (Fig. 5C–E).

3.5 Immune and Stromal Differences Between Risk Groups

CIBERSORT revealed significant group differences in plasma cells, resting memory CD4 T-cell, resting NK cells, M0 and M2 macrophages, resting dendritic cells, resting and activated mast cells, and eosinophils (Fig. 6A,B). ssGSEA additionally distinguished activated B-cell, activated CD4 T-cell, central memory CD8 T-cell, effector memory CD4 T-cell, eosinophil, immature B-cell, natural killer T-cell, natural killer-cell, neutrophil, and type 17 T-helper-cell scores (Fig. 6C). Immune estimates covaried across samples (Fig. 6D). Pathway analysis separated vascular-signaling and adhesion programs from fatty-acid oxidation, ketone-body metabolism, glucuronidation, and apoptotic signaling (Fig. 6E; **Supplementary Fig. 3**).

3.6 Genomic and Computational Immune Features of the Risk Groups

Mutation profiles for high- and low-risk tumors are presented in Fig. 7A,B. TMB was greater in the high-risk group, whereas the low-risk group had higher MSI scores (Fig. 7C,D). TIDE and T-cell dysfunction scores were also greater in high-risk tumors, but T-cell exclusion was comparable between groups (Fig. 7E–G). Risk status was associated with variation in several cancer-immunity-cycle steps (Fig. 7H) and with predicted sensitivity to several compounds (**Supplementary Fig. 4**). These computational measurements describe genomic and immune-context differences; they are not observations of clinical ICB response.

3.7 TIMP1 Expression, Survival, and Immune-Stromal Associations

Seven genes with positive risk coefficients were compared using tumor-normal expression, OS associations, model direction, and prior biological evidence. TIMP1 showed the most consistent combination of tumor upregulation and unfavorable survival. Previous studies link TIMP1

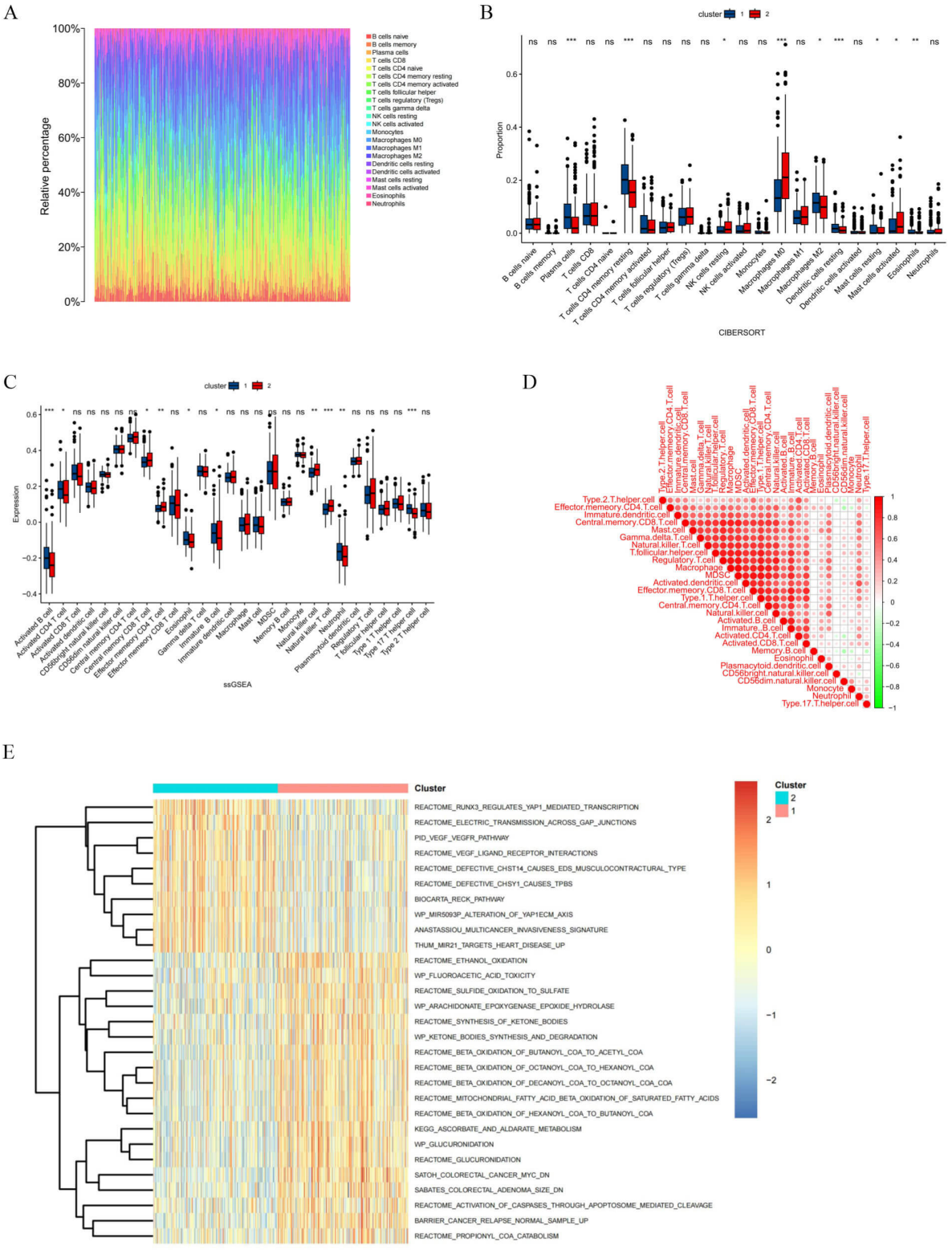


Fig. 6. Immune composition and pathway activity by risk group. (A) CIBERSORT-derived cell fractions across CRC samples. (B) Comparison of CIBERSORT estimates between clusters 1 and 2. (C) Comparison of ssGSEA immune-cell enrichment scores between clusters 1 and 2. (D) Pairwise correlations among ssGSEA immune-cell enrichment scores. (E) Heatmap of pathway activity scores across samples grouped by cluster. Wilcoxon tests were used in (B) (ns, not statistically significant, $*p < 0.05$, $**p < 0.01$, $***p < 0.001$). CIBERSORT, cell-type identification by estimating relative subsets of RNA transcripts; ssGSEA, single-sample gene set enrichment analysis.

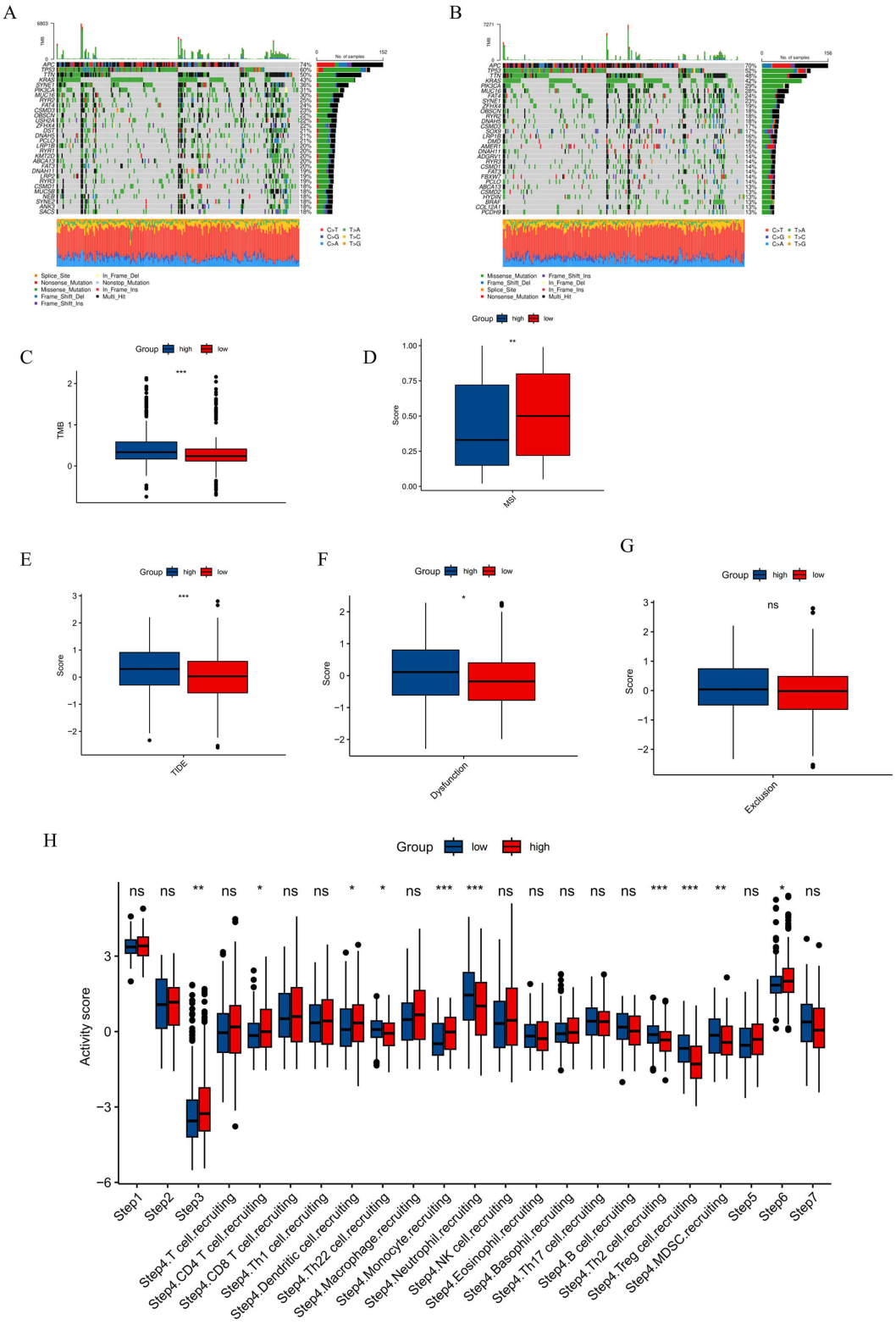


Fig. 7. Genomic and computational immune features by CRC risk group. (A,B) Somatic-mutation waterfalls for high-risk (A) and low-risk (B) tumors. (C) TMB. (D) MSI score. (E) TIDE score. (F) T-cell dysfunction. (G) T-cell exclusion, for which the groups did not differ significantly. (H) Cancer-immunity-cycle scores. Two-sided Wilcoxon rank-sum tests were used for group comparisons. In panels (C–G), blue and red represent the high-risk and low-risk groups, respectively. In panel (H), blue and red represent the low-risk and high-risk groups, respectively. ns, not statistically significant; *$p < 0.05$, **$p < 0.01$, ***$p < 0.001$. TMB, tumor mutational burden; MSI, microsatellite instability; TIDE, Tumor Immune Dysfunction and Exclusion.

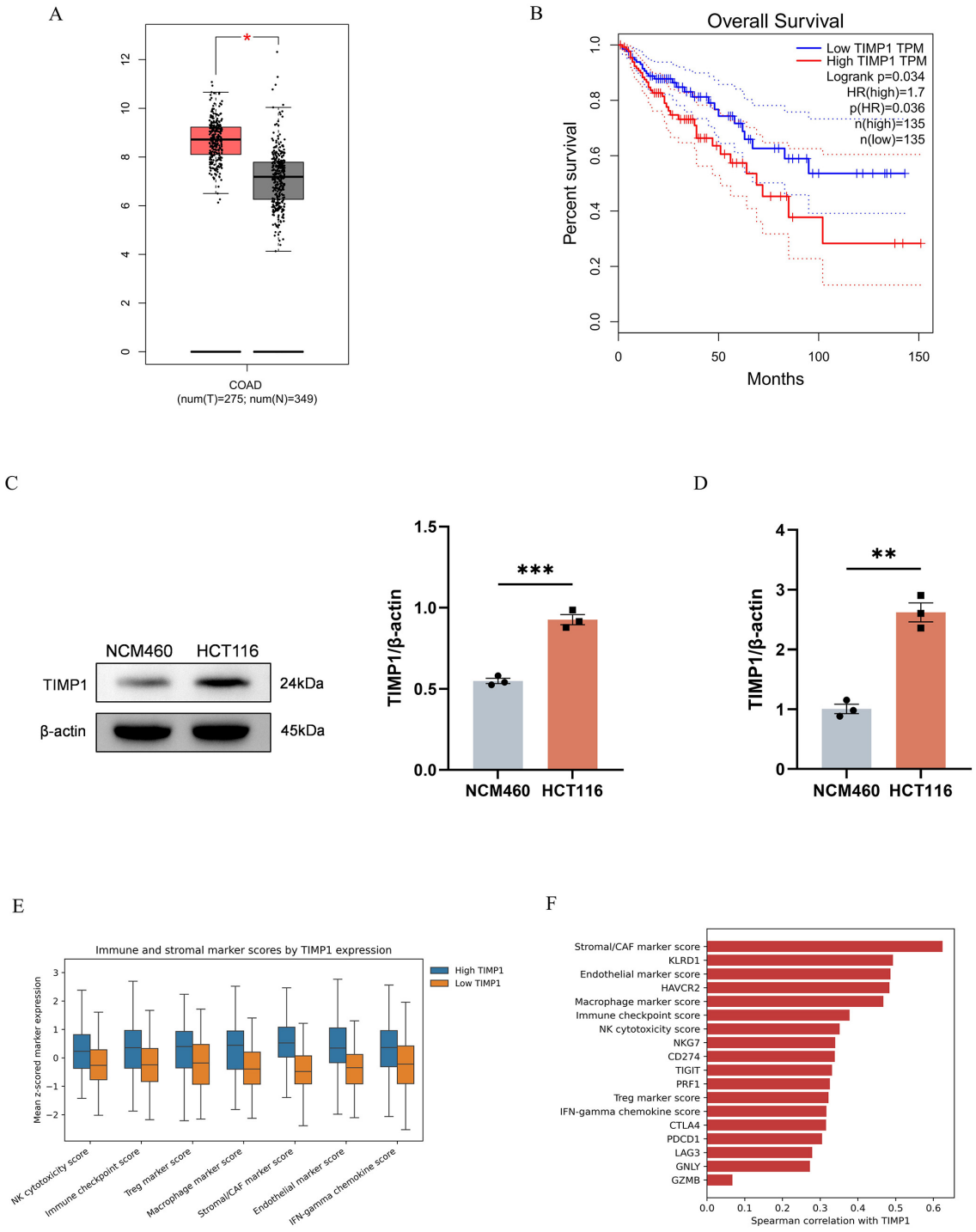


Fig. 8. TIMP1 expression, survival, and immune-stromal associations in CRC. (A) Expression in COAD tumors (red, n = 275) and normal tissues (gray, n = 349; Wilcoxon $p < 0.001$). (B) OS by TIMP1 expression group (log-rank $p = 0.034$; HR = 1.70, 95% CI 1.04–2.78). (C) Western blotting of total TIMP1 in NCM460 and HCT116 cells. (D) *TIMP1* qRT-PCR in the same cell lines; values are mean ± SD from three independent experiments. (E) Expression-derived immune and stromal scores by TIMP1 group. (F) Spearman correlations with marker scores and *KLRD1*, *HAVCR2*, *NKG7*, *CD274*, *TIGIT*, *PRF1*, *CTLA4*, *PDCD1*, *LAG3*, *GNLY*, and *GZMB* (*$p <$ 0.05, **$p < 0.01$, ***$p < 0.001$). COAD, colon adenocarcinoma; CI, confidence interval; qRT-PCR, quantitative real-time polymerase chain reaction; KLRD1, killer cell lectin like receptor D1; HAVCR2, hepatitis A virus cellular receptor 2; NKG7, natural killer cell granule protein 7; CD274, CD274 molecule (programmed death-ligand 1); TIGIT, T cell immunoreceptor with Ig and ITIM domains; PRF1, perforin 1; CTLA4, cytotoxic T-lymphocyte associated protein 4; PDCD1, programmed cell death 1; LAG3, lymphocyte activating 3; GNLY, granulysin; GZMB, granzyme B.

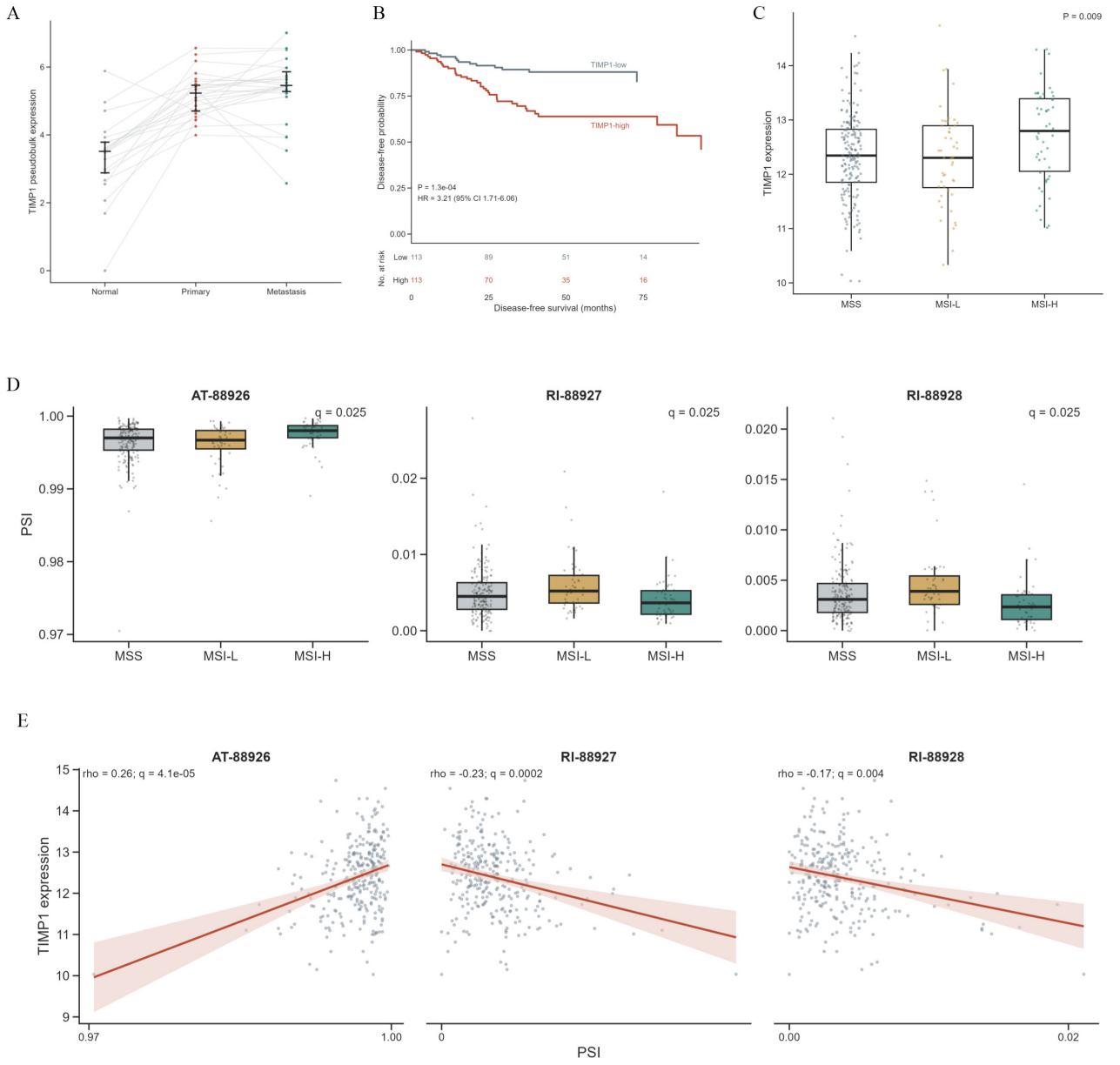


Fig. 9. External cohorts and MSI-related *TIMP1* measurements. (A) Patient-linked pseudobulk expression in normal colon, primary CRC, and metastases from HTAN-MSK. (B) DFS for *TIMP1*-high and *TIMP1*-low GSE14333 cases (n = 226; 50 recurrences), with the risk table shown. (C) Expression in MSS, MSI-L, and MSI-H TCGA-COAD tumors. (D) PSI of AT-88926, RI-88927, and RI-88928 by MSI category. (E) Event-level PSI versus total *TIMP1* expression; fitted trends are accompanied by 95% confidence bands. DFS, disease-free survival; MSS, microsatellite stable; MSI-L, microsatellite instability-low; MSI-H, microsatellite instability-high; PSI, percent spliced-in; HTAN-MSK, Memorial Sloan Kettering Cancer Center cohort of the Human Tumor Atlas Network; AT, alternate terminator; RI, retained intron. GSE14333 is a Gene Expression Omnibus (GEO) accession number.

to CRC detection, prognosis, fibroblast accumulation, invasion, and metastasis, and to angiogenesis in lung carcinoma [23,24,25,26,27,28,46]. The comparative results for S1PR5, TIMD4, XCL1, HSF4, ERFE, and NKX6-3 appear in **Supplementary Fig. 8**. These candidates also have biological relevance: S1PR5 mediates human NK-cell migration toward sphingosine-1-phosphate [47], NK-cell-derived XCL1 promotes recruitment of type 1 conventional dendritic cells (cDC1) into tumors [48], and Tim-4-expressing cavity-resident macrophages can impair antitumor CD8+ T-cell immunity [49]. NKX6-3, HSF4, and ERFE have been studied in other cancer settings [50,51,52]. TIMP1 was selected for further expression validation and cellular analysis.

COAD tumors expressed more TIMP1 than normal tissues (Fig. 8A). Patients with high TIMP1 expression

had shorter OS (log-rank p = 0.034; HR = 1.70, 95% confidence interval [CI] 1.04–2.78; Fig. 8B). HCT116 cells had higher total TIMP1 protein and mRNA levels than NCM460 cells (Fig. 8C,D). In bulk tumors, the TIMP1-high group had higher NK-cytotoxicity, immune-checkpoint, regulatory-T-cell, macrophage, stromal/CAF, endothelial, and interferon-gamma chemokine scores (Fig. 8E). TIMP1 expression correlated positively with stromal/CAF, endothelial, macrophage, and checkpoint scores, as well as several immune-regulatory or cytotoxic genes (Fig. 8F). These expression-based associations prompted analysis of TIMP1 across cellular compartments.

3.8 External TIMP1 Expression and Prognosis, With Secondary MSI and Splicing Analyses

Two independent cohorts were used to assess *TIMP1*. In HTAN-MSK [53], expression was greater in primary tumors than in matched normal colon (20 pairs; false discovery rate [FDR] q = 2.87×10^{-4}) and in metastases than in matched normal colon (19 pairs; q = 0.00156; Fig. 9A). Primary and metastatic specimens from the same patients did not differ significantly (25 pairs; q = 0.0758). In GSE14333 [54], recurrence risk increased with each standard-deviation rise in TIMP1 (HR = 1.74, 95% CI 1.28–2.36; $p = 4.14 \times 10^{-4}$). Median-defined *TIMP1*-high cases also had shorter DFS (HR = 3.21, 95% CI 1.71–6.06; log-rank $p = 1.35 \times 10^{-4}$; Fig. 9B).

TIMP1 abundance differed among the three MSI categories (p = 0.0092). MSI-H tumors had higher expression than MSS tumors (adjusted p = 0.0096) and MSI-L tumors (adjusted p = 0.0224; Fig. 9C).

Three *TIMP1* splice events were related to MSI. PSI for AT-88926, RI-88927, and RI-88928 varied across MSS, MSI-L, and MSI-H groups (FDR q = 0.025 for each; Fig. 9D). Relative to the other strata, MSI-H showed a small increase in AT-88926 PSI and decreases in the two retained-intron events.

The three MSI-associated events correlated with total *TIMP1* expression (Fig. 9E). AT-88926 showed a positive association (Spearman rho = 0.26; FDR q = 4.1×10^{-5}). Associations were negative for RI-88927 (rho = –0.23; q = 0.0002) and RI-88928 (rho = –0.17; q = 0.004). These event-level measurements describe MSI-associated transcript variation and are distinct from the external-cohort evidence for *TIMP1* expression and prognosis.

3.9 Cellular Distribution of TIMP1 and Predicted Intercellular Communication

We reanalyzed six primary CRC samples from GSE178318 to locate TIMP1 at single-cell resolution. Quality control and batch correction retained 55,735 cells for UMAP visualization (Fig. 10A). Canonical markers identified nine populations: B, endothelial, epithelial, mast, myeloid, NK, plasmacytoid dendritic, plasma, and T cells (Fig. 10B). The marker dot plot summarizes the fraction of positive cells and their mean expression (Fig. 10C). **Supplementary Fig. 5** contains the complete quality-control, dimensionality-reduction, variable-feature, and sample-composition outputs. TIMP1 was present in several populations and was comparatively abundant in NK, myeloid, and endothelial cells (Fig. 10D), indicating a distribution that extends beyond any single compartment.

CellChat predicted communication among epithelial, endothelial, myeloid, NK, T, and other cell populations (Fig. 10E). Selected ligand-receptor pairs are shown in Fig. 10F. The networks provide a multicellular context for TIMP1 expression but do not identify TIMP1-dependent communication.

3.10 Predicted TIMP1-Associated Responses and Transcriptional States in NK Cells

scTenifoldKnk simulated TIMP1 knockout in the annotated NK-cell subset. SEC61B, IRF8, PPP1R14B, GAS6, PLD4, TCF4, and JCHAIN were among the genes with the largest predicted responses (Fig. 11A). Seventy-seven genes, comprising the perturbation target TIMP1 and 76 other genes, satisfied |fold change| >2 and unadjusted $p < 0.05$ (**Supplementary Table 2**). Fig. 11A shows the 20 highest-ranked genes excluding TIMP1, whereas Fig. 11B summarizes the predicted perturbation Z-scores and significance. GO enrichment included leukocyte- and lymphocyte-mediated immunity, adaptive and humoral responses, antigen-receptor signaling, and lymphocyte proliferation (Fig. 11C; **Supplementary Table 3**). The PPI network summarized connectivity among the predicted responsive genes (Fig. 11D). KEGG analysis included phagocytosis, endoplasmic-reticulum protein processing, apoptosis, MAPK signaling, and antigen processing and presentation (**Supplementary Fig. 6**; **Supplementary Table 4**). These enrichments summarize a predicted network response, not an experimentally measured consequence of TIMP1 loss.

Monocle analysis placed TIMP1 expression along an inferred NK-cell trajectory. The continuous, branched structure indicated transcriptional heterogeneity within the annotated NK-cell population (Fig. 11E). The fitted TIMP1 expression trend increased nonlinearly toward late pseudotime (Fig. 11F). TIMP1-positive cells were concentrated in particular trajectory regions (Fig. 11G); additional state and ordering-gene plots are provided in **Supplementary Fig. 7**. This distribution relates TIMP1 expression to inferred cell states without establishing the direction of regulation or an effect on NK-cell homeostasis.

3.11 Exploratory Screening Identifies BRD-A98990573 for Experimental Testing

DrugReflector ranked BRD-A98990573 first in its zero-based output (rank 0; logit = 8.0635; probability = 0.02291). Fig. 12A shows the screening distribution with the 10 highest-ranked candidate compounds la-

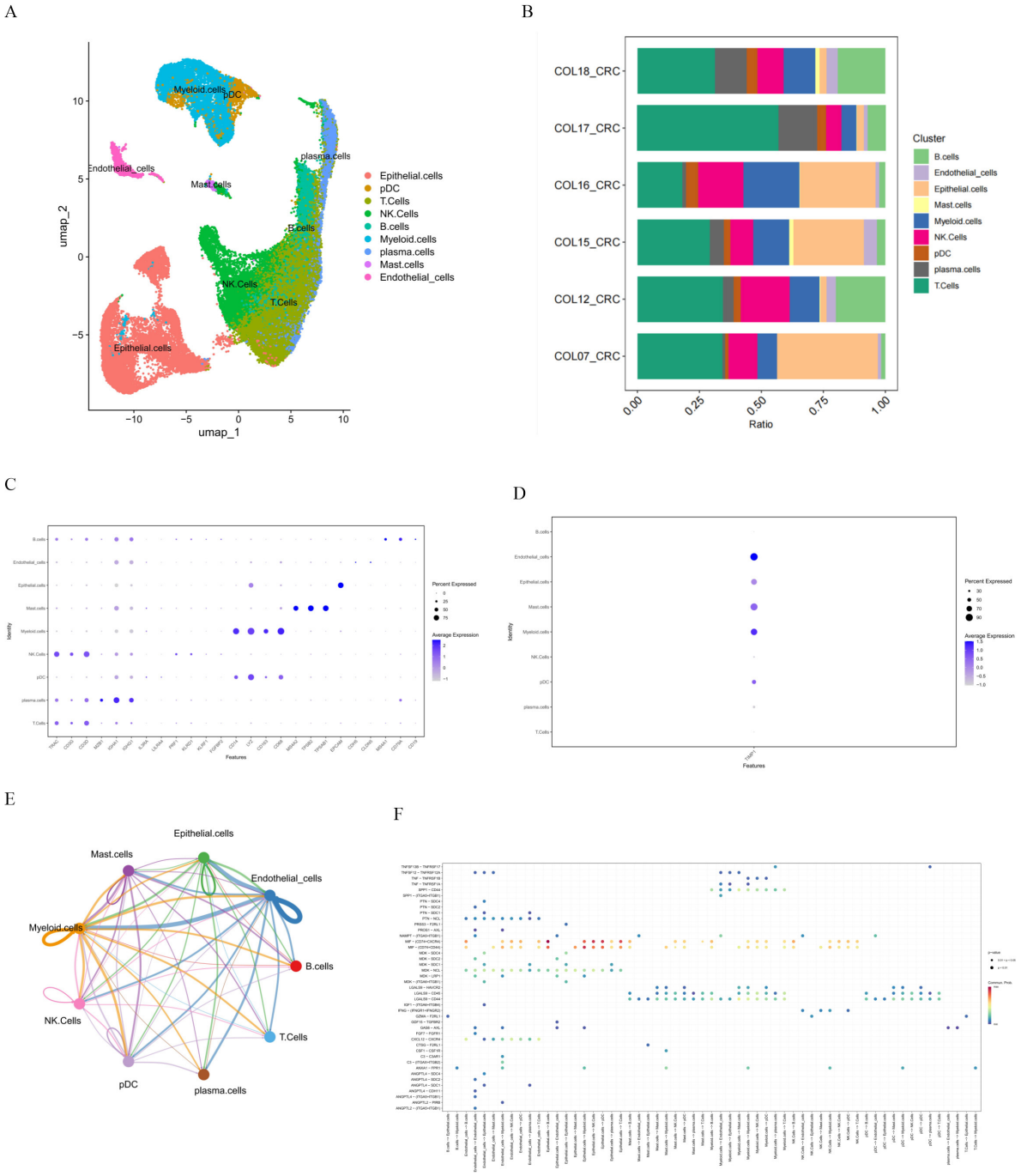


Fig. 10. Cellular distribution of *TIMP1* and inferred communication in CRC. (A) UMAP of 55,735 cells from six GSE178318 tumors. (B) Cell-type composition by sample. (C) Canonical-marker dot plot; dot area denotes the fraction of positive cells and color denotes mean expression. (D) *TIMP1* expression across annotated populations. (E) Global CellChat network; node size reflects outgoing-interaction number and edge width reflects predicted strength. (F) Selected ligand-receptor pairs. UMAP, uniform manifold approximation and projection.

beled, whereas **Supplementary Table 5** lists the 30 highest-ranked candidates. Docking generated a possible pose near TIMP1 HIS163 with an estimated energy of –3.818 kcal/-mol (Fig. 12B). The compound structure is shown in Fig. 12C.

4. Discussion

This study links TIMP1 expression to adverse outcomes and immune-stromal variation in CRC. The NK cell-related signature served as a starting point for candidate selection, rather than a direct measure of NK-cell function.

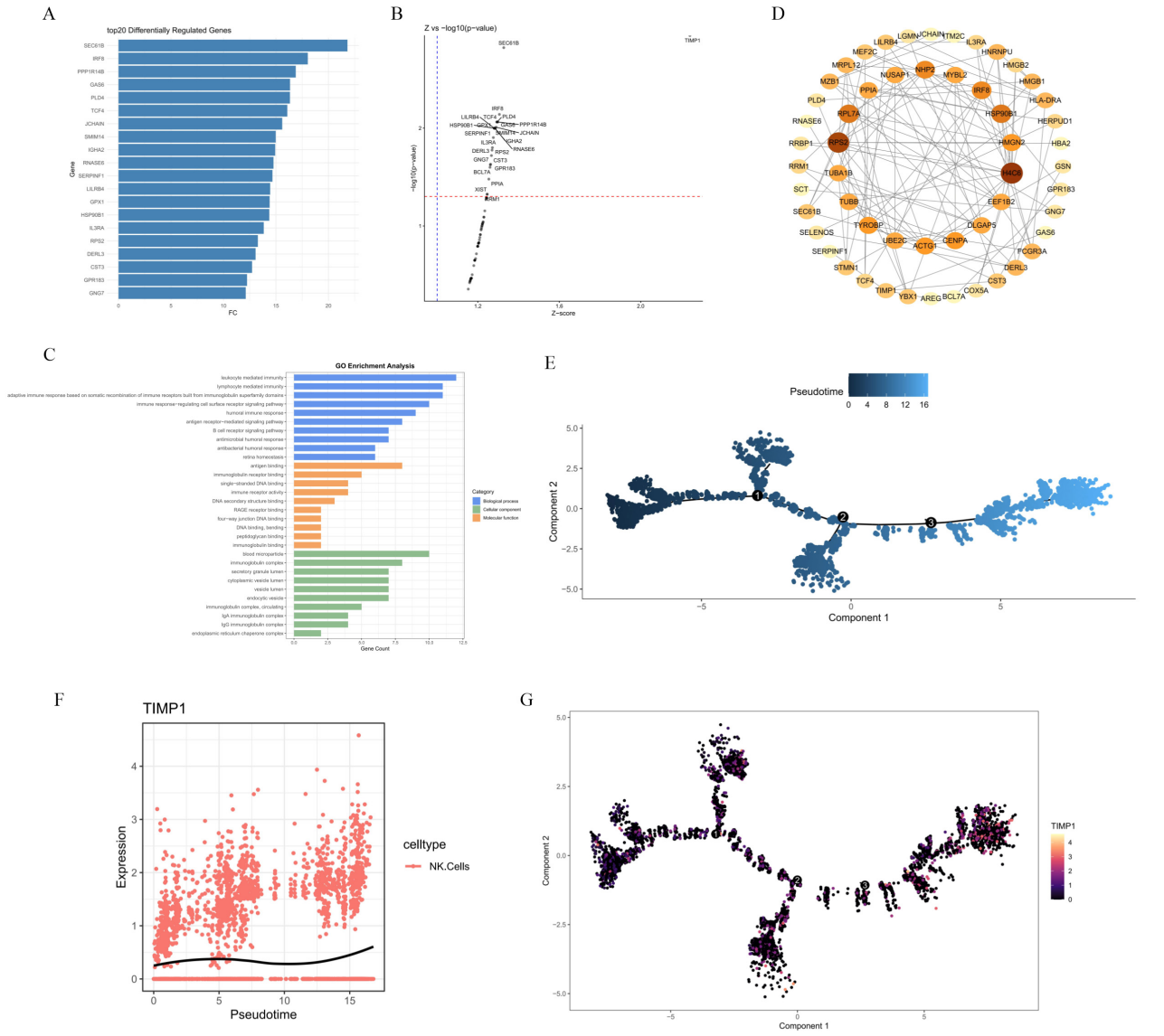


Fig. 11. Predicted responses to virtual TIMP1 knockout and NK-cell pseudotime. (A) Twenty genes with the largest predicted responses to simulated *TIMP1* removal, excluding the perturbation target TIMP1. (B) Predicted perturbation Z-scores and –log10(*p* values); dashed lines mark the thresholds. (C) GO enrichment within biological-process, cellular-component, and molecular-function domains. (D) PPI network of predicted responsive genes. (E) Monocle trajectory colored by inferred pseudotime, with numbered branch points. (F) Fitted *TIMP1* expression trend along pseudotime. (G) *TIMP1* expression projected onto the NK-cell trajectory. PPI, protein-protein interaction.

Independent cohorts supported the expression and prognostic associations, and cultured cells showed concordant differences in total TIMP1. Single-cell mapping then placed these findings within several cellular compartments. The contribution is therefore a clinically associated expression profile with cellular context, not evidence of a TIMP1–AS–NK regulatory axis.

The NK-cell focus complements CRC immunotherapy research centered on T-cell activation and exhaustion [10,11,12]. NK cells recognize stressed or MHC class I-altered targets without prior antigen-specific priming [13,14,15]. Here, NK-cell estimates varied alongside other immune, stromal, and genomic features. This broader variation argues against treating the signature as an NK-specific functional readout. Our findings instead describe immune environments in which NK cell-related transcription contributes to, but does not fully explain, the bulk expression pattern.

Higher immune-related scores alongside adverse prognosis need not imply effective antitumor immunity. Experimental studies have shown that NK cells can rapidly lose effector functions after entering tumors, reinforcing

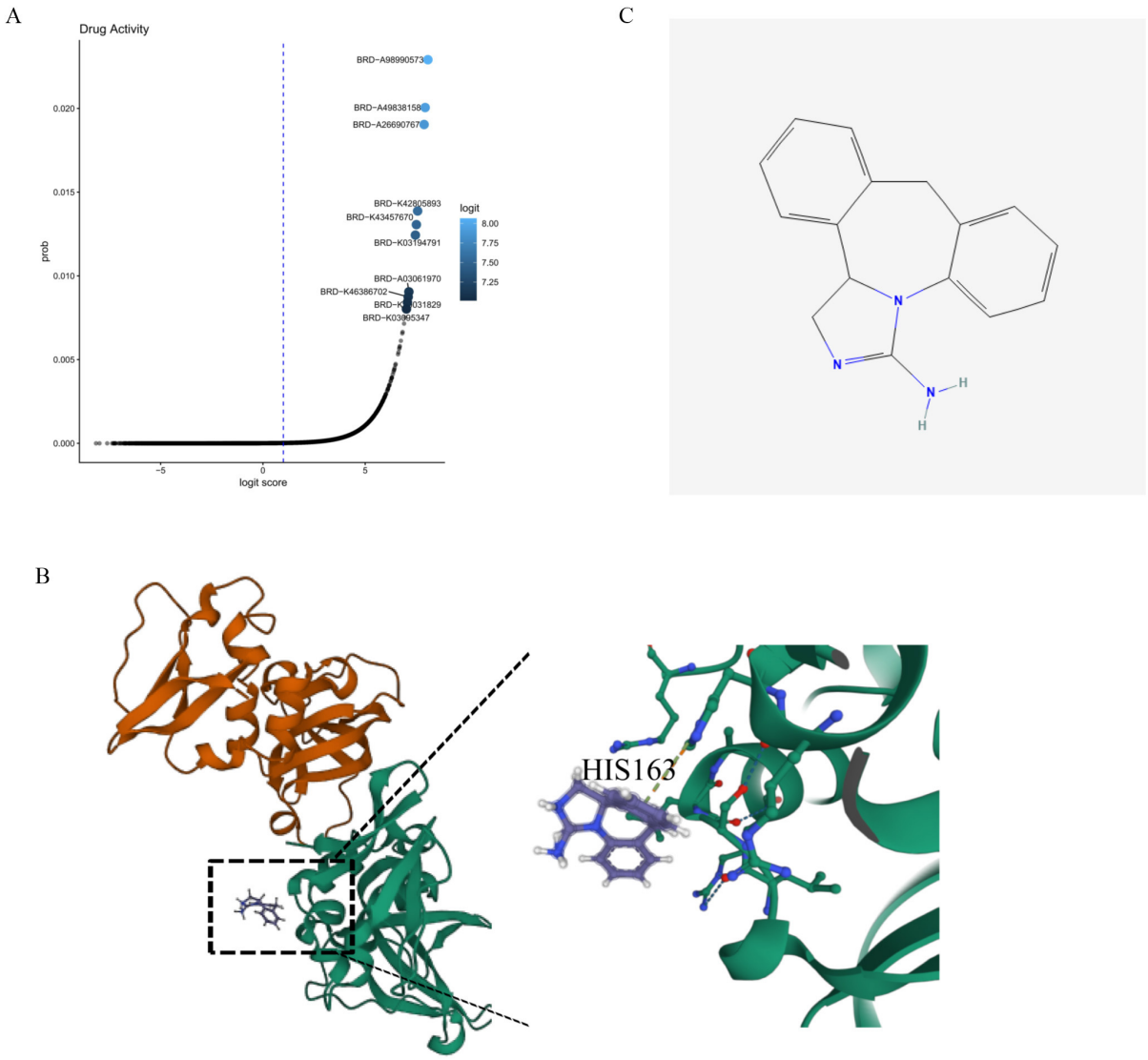


Fig. 12. Exploratory compound screening and docking of BRD-A98990573. (A) DrugReflector screening distribution with the 10 highest-ranked candidate compounds labeled; BRD-A98990573 ranked first (logit = 8.0635; probability = 0.02291). (B) Predicted pose near HIS163 in TIMP1 (PDB ID: 9SOQ; estimated energy, –3.818 kcal/mol). (C) Chemical structure of BRD-A98990573. PDB, Protein Data Bank; BRD-A98990573 is a Broad Institute compound identifier; HIS163 denotes histidine residue 163 in the protein structure.

the distinction between immune-cell infiltration and effective antitumor activity [55]. The scores may reflect recruitment of immune cells together with checkpoint expression, stromal accumulation, or altered cell composition. Experimental work in colorectal cancer has linked ASS1-dependent metabolic regulation to impaired CD8+ T-cell cytotoxicity, illustrating how tumor-intrinsic processes can contribute to immune evasion [56]. Bulk RNA measurements combine signals from these populations, so higher TIMP1 may reflect both cellular expression and the abundance of TIMP1-expressing cells. Single-cell and spatial transcriptomic analyses have also identified TIMP1-high mononuclear phagocytes within CRC tumors, supporting the need to consider myeloid-cell contributions when interpreting bulk TIMP1 expression [57]. The present analyses do not distinguish these explanations. Its multicellular distribution is consequently important for interpreting TIMP1-associated immune features, rather than attributing them to NK cells alone.

Earlier studies associated circulating or tissue TIMP1 with CRC detection and prognosis [25,26,27]. Experimental work also implicated TIMP1 in fibroblast accumulation, colorectal liver metastasis, proliferation, and invasion [23,24,28]. Recent experimental work further showed that CRC-derived TIMP1 promoted M2-like macrophage polarization and liver metastasis through CD63/beta1-integrin-AKT/mTOR signaling [58]. These macrophage-focused findings provide biological context for TIMP1-associated

immune heterogeneity but do not establish a TIMP1-NK-cell mechanism in our study. Our HTAN-MSK tissue comparisons [53] and GSE14333 survival analysis [54] provide concordant evidence in independent settings. The NCM460–HCT116 comparison supports a corresponding difference in total cellular expression. These observations strengthen the rationale for studying TIMP1 in CRC, but external-cohort concordance and cellular expression do not substitute for functional perturbation.

The distribution of TIMP1 does not establish which cells produce the clinically relevant signal or which populations respond to TIMP1. Single-cell profiling of Lynch syndrome-associated colorectal cancer has also revealed changes in epithelial and immune-cell composition and intercellular communication during disease progression [59]. Its distribution does not establish which cells produce the clinically relevant signal or which populations respond to TIMP1. Virtual knockout and pseudotime analysis identified predicted expression changes and cell-state associations within annotated NK cells. Humoral and immunoglobulin-related signals in the predicted response also warrant caution about cellular specificity. MSI-associated splice variation adds a separate descriptive finding, but the corresponding isoforms and their effects on NK cells were not tested. Thus, the expression, splicing, and single-cell observations should not be combined into a demonstrated mechanistic pathway.

BRD-A98990573 was identified by transcription-based screening and exploratory docking, not by an experimental assay of TIMP1 inhibition. Its predicted pose therefore does not establish binding, cellular activity, or isoform specificity. Direct binding measurements and dose-response assays with TIMP1 perturbation controls would distinguish target-related activity from nonspecific effects. Until those tests are available, the compound remains an exploratory candidate rather than a TIMP1 inhibitor.

5. Limitations

The clinical contribution is limited by the retrospective design and internal evaluation of the 11-gene signature. External cohorts assessed TIMP1 alone, so they do not establish the performance of the complete model in independent patients. More importantly, the cell experiments measured total TIMP1 in one normal colon and one CRC cell line, without functional or isoform-specific perturbation. They support an expression difference but cannot determine whether TIMP1 alters NK-cell activity or mediates the observed survival association. Testing these relationships requires controlled TIMP1 perturbation and tumor–NK cell interaction assays.

Cellular specificity also remains unresolved. The single-cell analysis included six tumors, and inferred communication, pseudotime, and virtual knockout depend on annotation and modeling assumptions. TIMP1 expression across several compartments leaves both cell composition and cell-intrinsic expression as possible explanations for its bulk associations. No ICB-treated cohort or experimental compound assessment was included, limiting conclusions about treatment response and therapeutic relevance. Independent model evaluation and cell-type-resolved functional studies would address these distinct clinical and biological uncertainties.

6. Conclusions

TIMP1 expression was associated with adverse prognosis and multicellular immune-stromal features in CRC. Independent cohorts and cellular measurements supported its expression differences, while single-cell analyses provided context that included NK cells. These findings prioritize TIMP1 for functional investigation, without establishing a splice-dependent NK-cell regulatory mechanism. Splicing and compound screening remain exploratory components of that investigation.

Abbreviations

AS, alternative splicing; AUC, area under the curve; CAF, cancer-associated fibroblast; CI, confidence interval; CIBERSORT, cell-type identification by estimating relative subsets of RNA transcripts; COAD, colon adenocarcinoma; CRC, colorectal cancer; dMMR, mismatch repair-deficient; DFS, disease-free survival; FDR, false discovery rate; FPKM, fragments per kilobase of transcript per million mapped reads; GO, Gene Ontology; HR, hazard ratio; ICB, immune checkpoint blockade; KEGG, Kyoto Encyclopedia of Genes and Genomes; LASSO, least absolute shrinkage and selection operator; MHC, major histocompatibility complex; MSI, microsatellite instability; MSI-H, microsatellite instability-high; MSI-L, microsatellite instability-low; MSS, microsatellite stable; NK, natural killer; OS, overall survival; PDB, Protein Data Bank; pMMR, mismatch repair-proficient; PPI, protein-protein interaction; PSI, percent spliced-in; qRT-PCR, quantitative real-time polymerase chain reaction; ROC, receiver operating characteristic; scRNA-seq, single-cell RNA sequencing; ssGSEA, single-sample gene set enrichment analysis; TCGA, The Cancer Genome Atlas; TCGASpliceSeq, The Cancer Genome Atlas SpliceSeq; TIDE, Tumor Immune Dysfunction and Exclusion; TMB, tumor mutational burden; TME, tumor microenvironment; t-SNE, t-distributed stochastic neighbor embedding; UMAP, uniform manifold approximation and projection; WGCNA, weighted gene co-expression network analysis; KLRD1, killer cell lectin like receptor D1; HAVCR2, hepatitis A virus cellular receptor 2; NKG7, natural killer cell granule protein 7; CD274, CD274 molecule (programmed death-ligand 1); TIGIT, T cell immunoreceptor with Ig and ITIM domains; PRF1, perforin 1; CTLA4, cytotoxic T-lymphocyte associated protein 4; PDCD1, programmed cell death 1; LAG3, lymphocyte activating 3; GNLY, granulysin; GZMB, granzyme B.

Availability of Data and Materials

The datasets analyzed in this study are publicly available. TCGA-COAD data were obtained from The Cancer Genome Atlas and cBioPortal. Alternative-splicing data were obtained from TCGASpliceSeq. The single-cell RNA-seq dataset was obtained from the Gene Expression Omnibus under accession number GSE178318, and the external prognostic dataset was obtained under accession number GSE14333. The HTAN-MSK CRC data were accessed through the cBioPortal study crc_hta8_htan_2024. Processed data supporting the findings are included in the manuscript and Supplementary Materials. Additional analysis tables and scripts are available from the corresponding authors upon reasonable request.

Author Contributions

ZZ, ZC, HL, MM, YG, BZ, HC, and ML contributed to the study. ZZ, BZ, HC, and ML conceived and designed the study. ZZ, ZC, HL, MM, and YG performed data curation and computational analyses. ZZ and ZC performed the statistical analyses and prepared the figures. ZZ performed the cell culture, western blotting, and qRT-PCR experiments. BZ, HC, and ML supervised the study. ZZ drafted the manuscript. All authors contributed to manuscript revision, read and approved the final version. All authors contributed to editorial changes in the manuscript. All authors have participated sufficiently in the work and agreed to be accountable for all aspects of the work.

Ethics Approval and Consent to Participate

This study analyzed publicly available, de-identified datasets and did not involve the prospective recruitment of human participants or the collection of identifiable human specimens. Therefore, ethics approval and written informed consent were not required under the applicable institutional and local requirements. The NCM460 and HCT116 cell lines used in this study were commercially available established cell lines.

Acknowledgment

The authors thank the developers and maintainers of The Cancer Genome Atlas, TCGASpliceSeq, cBioPortal, the Gene Expression Omnibus, and the HTAN-MSK project for making the relevant datasets publicly accessible.

Funding

This work was supported by the Science and Technology Program of Guangzhou (2025A03J3278 and 2025A04J3610), the Fostering Program for NSFC Young Applicants (Tulip Talent Training Program) of Sun Yat-sen University Cancer Center (2025yfd01).

Conflicts of Interest

The authors declare no conflicts of interest.

Declaration of AI and AI-Assisted Technologies in the Writing Process

During the preparation of this work, the authors used ChatGPT-5.5 in order to check spelling and grammar. After using this tool, the authors reviewed and edited the content as needed and take full responsibility for the content of the publication.

Supplementary Material

Supplementary material associated with this article can be found, in the online version, at https://doi.org/10.31083/FBL56745.

References

[1] Bray F, Laversanne M, Sung H, Ferlay J, Siegel RL, Soerjomataram I, et al. Global cancer statistics 2022: GLOBOCAN estimates of incidence and mortality worldwide for 36 cancers in 185 countries. CA: a Cancer Journal for Clinicians. 2024; 74: 229–263. https://doi.org/10.3322/caac.21834

[2] Dekker E, Tanis PJ, Vleugels JLA, Kasi PM, Wallace MB. Colorectal cancer. Lancet. 2019; 394: 1467–1480. https://doi.org/10.1016/S0140-6736(19)32319-0

[3] Cancer Genome Atlas Network. Comprehensive molecular characterization of human colon and rectal cancer. Nature. 2012; 487: 330–337. https://doi.org/10.1038/nature11252

[4] Agarwal P, Le DT, Boland PM. Immunotherapy in colorectal cancer. Advances in Cancer Research. 2021; 151: 137–196. https://doi.org/10.1016/bs.acr.2021.03.002

[5] Han S, Chok AY, Peh DYY, Ho JZM, Tan EKW, Koo SL, et al. The distinct clinical trajectory, metastatic sites, and immunobiology of microsatellite-instability-high cancers. Frontiers in Genetics. 2022; 13: 933475. https://doi.org/10.3389/fgene.2022.933475

[6] Le DT, Uram JN, Wang H, Bartlett BR, Kemberling H, Eyring AD, et al. PD-1 Blockade in Tumors with Mismatch-Repair Deficiency. The New England Journal of Medicine. 2015; 372: 2509–2520. https://doi.org/10.1056/NEJMoa1500596

[7] Diaz LA, Jr, Shiu KK, Kim TW, Jensen BV, Jensen LH, Punt C, et al. Pembrolizumab versus chemotherapy for microsatellite instability-high or mismatch repair-deficient metastatic colorectal cancer (KEYNOTE-177): final analysis of a randomised, open-label, phase 3 study. The Lancet. Oncology. 2022; 23: 659–670. https://doi.org/10.1016/S1470-2045(22)00197-8

[8] Overman MJ, McDermott R, Leach JL, Lonardi S, Lenz HJ, Morse MA, et al. Nivolumab in patients with metastatic DNA mismatch repair-deficient or microsatellite instability-high colorectal cancer (CheckMate 142): an open-label, multicentre, phase 2 study. The Lancet. Oncology. 2017; 18: 1182–1191. https://doi.org/10.1016/S1470-2045(17)30422-9

[9] André T, Lonardi S, Wong KYM, Lenz HJ, Gelsomino F, Aglietta M, et al. Nivolumab plus low-dose ipilimumab in previously treated patients with microsatellite instability-high/mismatch repair-deficient metastatic colorectal cancer: 4-year follow-up from CheckMate 142. Annals of Oncology. 2022; 33: 1052–1060. https://doi.org/10.1016/j.annonc.2022.06.008

[10] Wei SC, Levine JH, Cogdill AP, Zhao Y, Anang NAAS, Andrews MC, et al. Distinct Cellular Mechanisms Underlie Anti-CTLA-4 and Anti-PD-1 Checkpoint Blockade. Cell. 2017; 170: 1120–1133.e17. https://doi.org/10.1016/j.cell.2017.07.024

[11] Wei SC, Duffy CR, Allison JP. Fundamental Mechanisms of Immune Checkpoint Blockade Therapy. Cancer Discovery. 2018; 8: 1069–1086. https://doi.org/10.1158/2159-8290.CD-18-0367

[12] Chen DS, Mellman I. Oncology meets immunology: the cancer-

immunity cycle. Immunity. 2013; 39: 1–10. https://doi.org/10.1016/j.immuni.2013.07.012
[13] Vivier E, Raulet DH, Moretta A, Caligiuri MA, Zitvogel L, Lanier LL, et al. Innate or adaptive immunity? The example of natural killer cells. Science. 2011; 331: 44–49. https://doi.org/10.1126/science.1198687
[14] Freud AG, Mundy-Bosse BL, Yu J, Caligiuri MA. The Broad Spectrum of Human Natural Killer Cell Diversity. Immunity. 2017; 47: 820–833. https://doi.org/10.1016/j.immuni.2017.10.008
[15] Habif G, Crinier A, André P, Vivier E, Narni-Mancinelli E. Targeting natural killer cells in solid tumors. Cellular & Molecular Immunology. 2019; 16: 415–422. https://doi.org/10.1038/s41423-019-0224-2
[16] Qi J, Crinier A, Escalière B, Ye Y, Wang Z, Zhang T, et al. Single-cell transcriptomic landscape reveals tumor specific innate lymphoid cells associated with colorectal cancer progression. Cell Reports. Medicine. 2021; 2: 100353. https://doi.org/10.1016/j.xcrm.2021.100353
[17] Liu Y, Zhang Q, Xing B, Luo N, Gao R, Yu K, et al. Immune phenotypic linkage between colorectal cancer and liver metastasis. Cancer Cell. 2022; 40: 424–437.e5. https://doi.org/10.1016/j.ccell.2022.02.013
[18] Obino V, Giordano C, Carlomagno S, Setti C, Greppi M, Bozzo M, et al. Colorectal cancer-infiltrating NK cell landscape analysis unravels tissue-resident PD-1+ NK cells in microsatellite instability tumors. Frontiers in Immunology. 2025; 16: 1578444. https://doi.org/10.3389/fimmu.2025.1578444
[19] Han N, Liu Z. Targeting alternative splicing in cancer immunotherapy. Frontiers in Cell and Developmental Biology. 2023; 11: 1232146. https://doi.org/10.3389/fcell.2023.1232146
[20] Kahles A, Lehmann KV, Toussaint NC, Hüser M, Stark SG, Sachsenberg T, et al. Comprehensive Analysis of Alternative Splicing Across Tumors from 8,705 Patients. Cancer Cell. 2018; 34: 211–224.e6. https://doi.org/10.1016/j.ccell.2018.07.001
[21] Frankiw L, Baltimore D, Li G. Alternative mRNA splicing in cancer immunotherapy. Nature Reviews. Immunology. 2019; 19: 675–687. https://doi.org/10.1038/s41577-019-0195-7
[22] Shi JY, Bi YY, Yu BF, Wang QF, Teng D, Wu DN. Alternative Splicing Events in Tumor Immune Infiltration in Colorectal Cancer. Frontiers in Oncology. 2021; 11: 583547. https://doi.org/10.3389/fonc.2021.583547
[23] Gong Y, Scott E, Lu R, Xu Y, Oh WK, Yu Q. TIMP-1 promotes accumulation of cancer associated fibroblasts and cancer progression. PloS One. 2013; 8: e77366. https://doi.org/10.1371/journal.pone.0077366
[24] Ma B, Ueda H, Okamoto K, Bando M, Fujimoto S, Okada Y, et al. TIMP1 promotes cell proliferation and invasion capability of right-sided colon cancers via the FAK/Akt signaling pathway. Cancer Science. 2022; 113: 4244–4257. https://doi.org/10.1111/cas.15567
[25] Lee JH, Choi JW, Kim YS. Plasma or serum TIMP-1 is a predictor of survival outcomes in colorectal cancer: a meta-analysis. Journal of Gastrointestinal and Liver Diseases. 2011; 20: 287–291.
[26] Meng C, Yin X, Liu J, Tang K, Tang H, Liao J. TIMP-1 is a novel serum biomarker for the diagnosis of colorectal cancer: A meta-analysis. PloS One. 2018; 13: e0207039. https://doi.org/10.1371/journal.pone.0207039
[27] Böckelman C, Beilmann-Lehtonen I, Kaprio T, Koskensalo S, Tervahartiala T, Mustonen H, et al. Serum MMP-8 and TIMP-1 predict prognosis in colorectal cancer. BMC Cancer. 2018; 18: 679. https://doi.org/10.1186/s12885-018-4589-x
[28] Rao VS, Gu Q, Tzschentke S, Lin K, Ganig N, Thepkaysone ML, et al. Extravesicular TIMP-1 is a non-invasive independent prognostic marker and potential therapeutic target in colorectal liver metastases. Oncogene. 2022; 41: 1809–1820. https://doi.org/10.1038/s41388-022-02218-9
[29] Ryan M, Wong WC, Brown R, Akbani R, Su X, Broom B, et al. TCGASpliceSeq a compendium of alternative mRNA splicing in cancer. Nucleic Acids Research. 2016; 44: D1018–D1022. https://doi.org/10.1093/nar/gkv1288
[30] Langfelder P, Horvath S. WGCNA: an R package for weighted correlation network analysis. BMC Bioinformatics. 2008; 9: 559. https://doi.org/10.1186/1471-2105-9-559
[31] Simon N, Friedman J, Hastie T, Tibshirani R. Regularization Paths for Cox's Proportional Hazards Model via Coordinate Descent. Journal of Statistical Software. 2011; 39: 1–13. https://doi.org/10.18637/jss.v039.i05
[32] Friedman J, Hastie T, Tibshirani R. Regularization Paths for Generalized Linear Models via Coordinate Descent. Journal of Statistical Software. 2010; 33: 1–22. https://doi.org/10.18637/jss.v033.i01
[33] Newman AM, Liu CL, Green MR, Gentles AJ, Feng W, Xu Y, et al. Robust enumeration of cell subsets from tissue expression profiles. Nature Methods. 2015; 12: 453–457. https://doi.org/10.1038/nmeth.3337
[34] Hänzelmann S, Castelo R, Guinney J. GSVA: gene set variation analysis for microarray and RNA-seq data. BMC Bioinformatics. 2013; 14: 7. https://doi.org/10.1186/1471-2105-14-7
[35] Mayakonda A, Lin DC, Assenov Y, Plass C, Koeffler HP. Maftools: efficient and comprehensive analysis of somatic variants in cancer. Genome Research. 2018; 28: 1747–1756. https://doi.org/10.1101/gr.239244.118
[36] Jiang P, Gu S, Pan D, Fu J, Sahu A, Hu X, et al. Signatures of T cell dysfunction and exclusion predict cancer immunotherapy response. Nature Medicine. 2018; 24: 1550–1558. https://doi.org/10.1038/s41591-018-0136-1
[37] Che LH, Liu JW, Huo JP, Luo R, Xu RM, He C, et al. A single-cell atlas of liver metastases of colorectal cancer reveals reprogramming of the tumor microenvironment in response to preoperative chemotherapy. Cell Discovery. 2021; 7: 80. https://doi.org/10.1038/s41421-021-00312-y
[38] Stuart T, Butler A, Hoffman P, Hafemeister C, Papalexi E, Mauck WM, 3rd, et al. Comprehensive Integration of Single-Cell Data. Cell. 2019; 177: 1888–1902.e21. https://doi.org/10.1016/j.cell.2019.05.031
[39] Korsunsky I, Millard N, Fan J, Slowikowski K, Zhang F, Wei K, et al. Fast, sensitive and accurate integration of single-cell data with Harmony. Nature Methods. 2019; 16: 1289–1296. https://doi.org/10.1038/s41592-019-0619-0
[40] Osorio D, Zhong Y, Li G, Xu Q, Yang Y, Tian Y, et al. scTenifoldKnk: An efficient virtual knockout tool for gene function predictions via single-cell gene regulatory network perturbation. Patterns. 2022; 3: 100434. https://doi.org/10.1016/j.patter.2022.100434
[41] Jin S, Guerrero-Juarez CF, Zhang L, Chang I, Ramos R, Kuan CH, et al. Inference and analysis of cell-cell communication using CellChat. Nature Communications. 2021; 12: 1088. https://doi.org/10.1038/s41467-021-21246-9
[42] Trapnell C, Cacchiarelli D, Grimsby J, Pokharel P, Li S, Morse M, et al. The dynamics and regulators of cell fate decisions are revealed by pseudotemporal ordering of single cells. Nature Biotechnology. 2014; 32: 381–386. https://doi.org/10.1038/nbt.2859
[43] Qiu X, Mao Q, Tang Y, Wang L, Chawla R, Pliner HA, et al. Reversed graph embedding resolves complex single-cell trajectories. Nature Methods. 2017; 14: 979–982. https://doi.org/10.1038/nmeth.4402
[44] DeMeo B, Nesbitt C, Miller SA, Burkhardt DB, Lipchina I, Fu D, et al. Active learning framework leveraging transcriptomics identifies modulators of disease phenotypes. Science. 2025; 390:

eadi8577. https://doi.org/10.1126/science.adi8577
[45] Eberhardt J, Santos-Martins D, Tillack AF, Forli S. AutoDock Vina 1.2.0: New Docking Methods, Expanded Force Field, and Python Bindings. Journal of Chemical Information and Modeling. 2021; 61: 3891–3898. https://doi.org/10.1021/acs.jcim.1c00203
[46] Rojiani MV, Ghoshal-Gupta S, Kutiyanawalla A, Mathur S, Rojiani AM. TIMP-1 overexpression in lung carcinoma enhances tumor kinetics and angiogenesis in brain metastasis. Journal of Neuropathology and Experimental Neurology. 2015; 74: 293–304. https://doi.org/10.1097/NEN.0000000000000175
[47] Drouillard A, Mathieu AL, Marçais A, Belot A, Viel S, Mingueneau M, et al. S1PR5 is essential for human natural killer cell migration toward sphingosine-1 phosphate. The Journal of Allergy and Clinical Immunology. 2018; 141: 2265–2268.e1. https://doi.org/10.1016/j.jaci.2017.11.022
[48] Böttcher JP, Bonavita E, Chakravarty P, Blees H, Cabeza-Cabrerizo M, Sammicheli S, et al. NK Cells Stimulate Recruitment of cDC1 into the Tumor Microenvironment Promoting Cancer Immune Control. Cell. 2018; 172: 1022–1037.e14. https://doi.org/10.1016/j.cell.2018.01.004
[49] Chow A, Schad S, Green MD, Hellmann MD, Allaj V, Ceglia N, et al. Tim-4+ cavity-resident macrophages impair anti-tumor CD8+ T cell immunity. Cancer Cell. 2021; 39: 973–988.e9. https://doi.org/10.1016/j.ccell.2021.05.006
[50] Yoon JH, Choi WS, Kim O, Choi SS, Lee EK, Nam SW, et al. NKX6.3 controls gastric differentiation and tumorigenesis. Oncotarget. 2015; 6: 28425–28439. https://doi.org/10.18632/oncotarget.4952
[51] Yang Y, Jin L, Zhang J, Wang J, Zhao X, Wu G, et al. High HSF4 expression is an independent indicator of poor overall survival and recurrence free survival in patients with primary colorectal cancer. IUBMB Life. 2017; 69: 956–961. https://doi.org/10.1002/iub.1692
[52] Xu Q, Altrock E, Schmitt N, Streuer A, Rapp F, Nowak V, et al. In Silico Pan-Cancer Analysis Reveals Prognostic Role of the Erythroferrone (ERFE) Gene in Human Malignancies. International Journal of Molecular Sciences. 2023; 24: 1725. https://doi.org/10.3390/ijms24021725
[53] Moorman A, Benitez EK, Cambuli F, Jiang Q, Mahmoud A, Lumish M, et al. Progressive plasticity during colorectal cancer metastasis. Nature. 2025; 637: 947–954. https://doi.org/10.1038/s41586-024-08150-0
[54] Jorissen RN, Gibbs P, Christie M, Prakash S, Lipton L, Desai J, et al. Metastasis-Associated Gene Expression Changes Predict Poor Outcomes in Patients with Dukes Stage B and C Colorectal Cancer. Clinical Cancer Research. 2009; 15: 7642–7651. https://doi.org/10.1158/1078-0432.CCR-09-1431
[55] Dean I, Lee CYC, Tuong ZK, Li Z, Tibbitt CA, Willis C, et al. Rapid functional impairment of natural killer cells following tumor entry limits anti-tumor immunity. Nature Communications. 2024; 15: 683. https://doi.org/10.1038/s41467-024-44789-z
[56] Sun L, Fu D, Zhang H. ASS1 Promotes Colorectal Cancer Immune Evasion Through CPT1A-Mediated S100A10 Succinylation. Frontiers in Bioscience-Landmark. 2026; 31: 48764. https://doi.org/10.31083/FBL48764
[57] Ji T, Fu H, Wang L, Chen J, Tian S, Wang G, et al. Single-cell RNA profiling reveals classification and characteristics of mononuclear phagocytes in colorectal cancer. PLOS Genetics. 2024; 20: e1011176. https://doi.org/10.1371/journal.pgen.1011176
[58] Liu J, Zhao L, Wang L, Sheng G, Cheng P, Han M, et al. Integrin-Mediated TIMP1 Signaling Reprograms Liver Macrophages and Accelerates Colorectal Cancer Metastasis. Cells. 2025; 15: 29. https://doi.org/10.3390/cells15010029
[59] Chen S, Feng J, Fang Z, Jiang Y, Duanmu J, Yu X, et al. From Normal Mucosa to Colorectal Cancer in Lynch Syndrome: Single-Cell Dissection of Cellular Heterogeneity and Communication Networks. Frontiers in Bioscience-Landmark. 2026; 31: 47730. https://doi.org/10.31083/FBL47730